Available online at www.sciencedirect.com
ScienceDirect
Geochimica et Cosmochimica Acta 71 (2007) 5203–5225
Geochimica et Cosmochimica Acta
www.elsevier.com/locate/gca

Mechanism and timing of lithospheric modification and replacement beneath the eastern North China Craton: Peridotitic xenoliths from the 100 Ma Fuxin basalts and a regional synthesis

J.P. Zheng [a,b,*], W.L. Griffin [b], S.Y. O'Reilly [b], C.M. Yu [a], H.F. Zhang [c], N. Pearson [b], M. Zhang [b]

[a] *State Key Laboratory of Geological Process and Mineral Resources, Faculty of Earth Sciences, China University of Geosciences, Wuhan 430074, China*
[b] *GEMOC ARC National Key Centre, Department of Earth and Planetary Sciences, Macquarie University, Sydney, NSW 2109, Australia*
[c] *Institute of Geology and Geophysics, Chinese Academy of Sciences, Beijing 100029, China*

Received 15 March 2007; accepted in revised form 24 July 2007; available online 8 September 2007

Abstract

Lithospheric thinning beneath the eastern North China Craton is widely recognized, but the mechanism and timing of the thinning are contentious. New data on peridotitic xenoliths from the Cretaceous (~100 Ma) Fuxin basalts at the northern edge of the craton have been integrated with data from other localities across the craton, to provide an overview of the processes involved. The Fuxin peridotite xenoliths can be subdivided into three types, which can also be recognized in other xenolith suites across the craton. The dominant Type 1, lherzolites with olivine $Mg^{\#}$ ~90, represents fertile mantle (5–12% partial-melt extraction) that makes up much of the Late Mesozoic–Cenozoic lithosphere beneath the craton. Type 2 consists of magnesian (olivine $Mg^{\#}$ >92) harzburgites, interpreted as shallow relics of the Archean cratonic mantle. Type 3, minor lherzolite xenoliths with olivine $Mg^{\#}$ ~86 reflect the interaction of the lithosphere with magmas similar to the host basalts. In-situ Re–Os data on sulfides in xenoliths from Hebi (4 Ma, interior of the craton) and Hannuoba (22 Ma, northern edge of the Trans-North China Orogen within the craton) basalts give model ages of 3.1–3.0, 2.5, 2.2–2.1, 1.4 and 0.8 Ga, These correspond to the U–Pb ages of zircons from early Mesozoic (178 Ma) peridotitic xenoliths at the southern margin of the craton, and record events during which the Archean lithospheric mantle was modified. The dominance of fertile peridotite xenoliths in the 100 Ma Fuxin basalts indicates that the mantle replacement beneath the eastern North China Craton at least partly took place before that time. The regional synthesis suggests that Mesozoic–Cenozoic lithospheric thinning and mantle replacement was heterogeneously distributed across the North China Craton in space and time. Lateral spreading of the lithosphere, accompanied by asthenospheric upwelling and melt–peridotite interaction, is the most probable mechanism for the lithospheric thinning beneath the eastern part of the craton. Subsequent cooling of the upwelled asthenosphere caused some re-thickening of the lithosphere; this overall more fertile and hence denser lithosphere resulted in widespread basin formation.

1. INTRODUCTION

Refractory mantle roots, often preserved beneath cratons due to their inherent buoyancy and high viscosity (Griffin et al., 1999b), can be modified or even finally replaced by more fertile materials through asthenosphere–lithosphere

* Corresponding author. Fax: +86 27 67883873.
E-mail address: jpzheng2003@yahoo.com (J.P. Zheng).

0016-7037/$ - see front matter © 2007 Elsevier Ltd. All rights reserved.
doi:10.1016/j.gca.2007.07.028

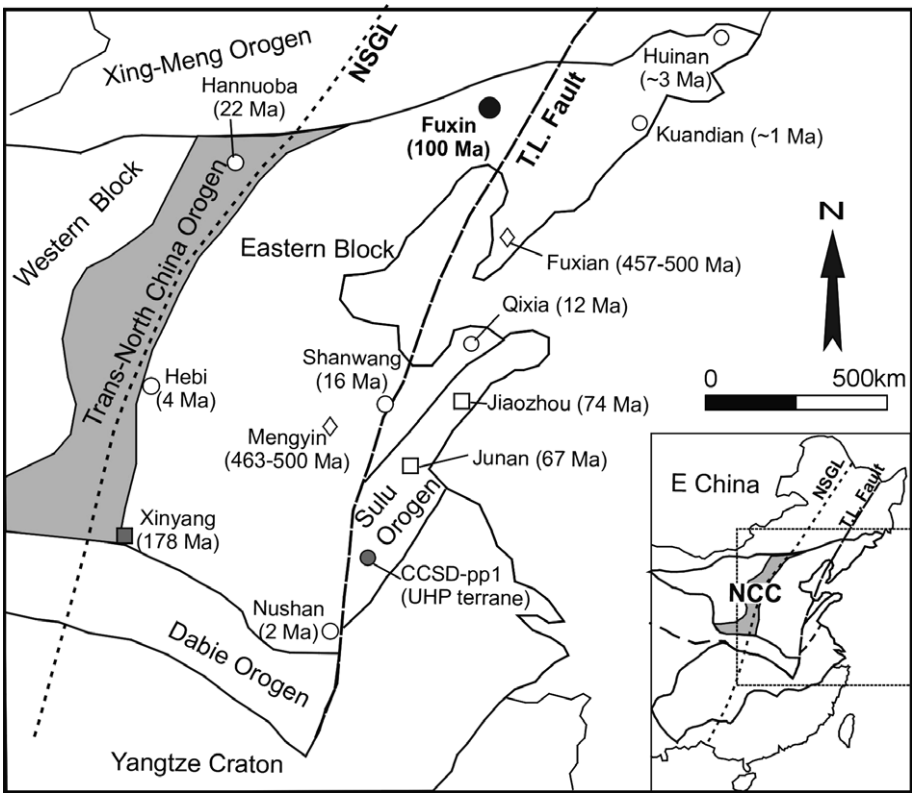

Fig. 1. Locations of some peridotite outcrops and xenolith-bearing igneous rocks in eastern North China. Data in brackets represent the eruption ages of the xenolith-bearing rocks. NCC, North China Craton; CCSD-pp1, pre-pilot hole of the Chinese Continental Scientific Drilling Project in the Sulu ultrahigh-high pressure (UHP) terrane; NSGL, North–South Gravity Lineament; T.L. Fault, Tan-Lu translithospheric fault zone.

interaction (Zheng, 1999; O'Reilly et al., 2001). The North China Craton (NCC) is one of the major Archean cratons in eastern Eurasia and contains rocks $\geqslant$3.6 Ga old (Liu et al., 1992; Zheng et al., 2004a). Peridotite xenoliths from Paleozoic diamond-bearing kimberlites within the craton represent samples of an ancient refractory mantle lithosphere which was thick (ca. 200 km) and cold (geotherm ca. 40 mW/m^2) at least up to mid-Ordovician time (Zheng and Lu, 1999). In contrast, peridotites from basalts erupted at $\leqslant$74 Ma show a thin (<90 km), hot (mean geotherm ca. 80 mW/m^2) and compositionally heterogeneous lithosphere beneath the same area (Xu et al., 1995a, 1998; Zheng et al., 1998, 2001; Chen et al., 2001). These observations suggest that more than 100 km of cratonic lithosphere was removed or strongly modified during late Mesozoic–Cenozoic time (Fan and Menzies, 1992; Griffin et al., 1992, 1998b; Menzies et al., 1993; Zheng, 1999; Gao et al., 2002; Zhang et al., 2004, 2007a). The mechanism of lithospheric thinning has been interpreted in terms of either asthenospheric erosion (Griffin et al., 1992, 1998b; Menzies and Xu, 1998; Xu et al., 1998; Zheng et al., 1998; Fan et al., 2001; Xu, 2001, 2007) or lithospheric delamination (Wu et al., 2003; Deng et al., 2004; Gao et al., 2004). The initiation of the thinning process has been considered as Early Mesozoic (Zheng et al., 2006a), Late Mesozoic (Xu, 2001; Menzies et al., 2007) or Tertiary (Menzies et al., 1993).

Here we present detailed petrography and mineral chemistry data for a series of peridotitic xenoliths from the Cretaceous (~100 Ma) Fuxin alkali basalts at the northern edge of the North China Craton (Fig. 1). In-situ Re–Os dating of sulfides in peridotite xenoliths from the Hebi and Hannuoba localities is also presented. To place these data in a regional context, we review published compositional data for peridotitic xenoliths from Paleozoic (457–500 Ma, Mengyin and Fuxian), early Mesozoic (178 Ma, Xinyang), late Mesozoic (~70 Ma, Jiaozhou and Junan) and Cenozoic (<22 Ma, Hannuoba, Shanwang, Qixia, Hebi, Huinan, Nushan and Kuandian) localities within the craton, and for Triassic (~220 Ma) peridotite massifs (CCSD-pp1) in the Sulu ultrahigh-pressure (UHP) belt along the southern edge of the craton. Our aims are: (1) to characterize the nature of the lithospheric mantle beneath the craton from Paleozoic to Cenozoic time and (2) to constrain the mechanism, initiation and progress of lithospheric modification and replacement beneath the eastern North China Craton.

2. GEOLOGICAL SETTING AND PETROGRAPHY

The North China Craton (NCC) is bounded by the Xing-Meng Orogen on the north and the Dabie–Sulu Orogen on the south (Fig. 1). The oldest known rocks are

Table 1
Microstructure and mode of the Fuxin peridotite xenoliths from the North China Craton

Type	Sample	Rock	Microstructure	Mg# in Ol	Cr# in Sp	F (%)	Mode (%)			
							Ol	Opx	Cpx	Sp
Type 1	JG6	Spinel lherzolite	Porphyroclastic	90.7	26.5	10.7	61.0	31.2	6.3	1.5
	JG17	Spinel lherzolite	Porphyroclastic	90.3	34.5	13.4	60.5	32.6	5.8	1.1
	JG18	Spinel lherzolite	Porphyroclastic	90.3	29.5	11.8	59.7	31.4	5.6	3.3
	JG19	Spinel lherzolite	Porphyroclastic	90.1 (C)–86.7 (R)	18.5	7.1	57.1	28.6	11.2	3.1
	JG20	Spinel lherzolite	Porphyroclastic	90.3	14.7	4.8	61.2	33.2	5.2	0.4
	JG26	Spinel lherzolite	Porphyroclastic	90.5	28.5	11.4	58.4	34.8	5.6	1.2
	JG27	Spinel lherzolite	Porphyroclastic	90.5	28.5	11.4	59.1	29.4	8.6	2.9
	JG28	Spinel lherzolite	Porphyroclastic	90.4	29.4	11.8	59.3	31.7	6.3	2.7
	JG29	Spinel lherzolite	Porphyroclastic	90.2	14.7	4.8	58.7	31.3	7.9	2.1
	JG15	Spinel dunite	Coarse	88.9	49.5	17.0	98.3			1.7
Type 2	JG23	Spinel harzburgite	Coarse	92.2	58.7	18.7	68.2	31.6	Free	0.2
	JG32	Spinel harzburgite	Coarse	92.1	58.8	18.7	65.8	33.9	Free	0.3
Type 3	JG10	Spinel lherzolite	Porphyroclastic	86.5	39.0	14.6	55.7	28.8	12.4	3.1
	JG12	Lherzolite	Porphyroclastic	84.4			60.3	31.0	8.7	
	JG13-1	Spinel lherzolite	Porphyroclastic	86.0	38.8	14.5	58.2	29.8	9.7	2.3
	JG13-2	Spinel lherzolite	Porphyroclastic	86.4			59.0	32.3	8.7	
Hebi ($n = 32$)	High Mg	Sp harzburgite	Main coarse	92.1 (91.3–92.8)[a]	55.0 (45.9–63.0)	17.8 (16.2–19.4)	71.8 (58.2–85.5)	26.8 (15.3–40.8)	3.1 (0.5–6.4)	1.2 (0.0–5.0)
Hebi ($n = 3$)	Low Mg	Sp lherzolite	Main coarse	90.1 (88.6–90.4)	23.5(20.3–26.8)	9.5 (8.1–10.8)	70.2 (65.1–83.0)	27.8 (16.5–33.5)	10.1 (5.8–16.5)	1.1 (0.5–1.5)
TLFZ ($n = 49$)		Sp–Gnt lherzolite	Fine-porphyroclastic	89.4 (87.4–90.6)	16.5 (11.0–23.0)	5.6 (1.2–9.3)	63.6 (38.0–82.3)	24.3 (6.8–38.2)	8.2 (3.4–19.5)	2.7 (0.6–5.5)

Hebi, high: Mg# group, refractory mantle in the Archean North China Craton (Zheng et al., 2001).
TLFZ, translithospheric fault zone areas including Shanwang (Zheng et al., 1998) and Nushan (Xu et al., 1998) in the Tanlu fault within the North China Craton.
C, core; R, rim; F (%), calculated after the method of Hellebrand et al. (2001).
[a] Average (range).

⩾3.6 Ga old (Liu et al., 1992; Zheng et al., 2004a), and the craton underwent a series of tectonic events in the late Archean and Paleoproterozoic (Zheng et al., 2004b); it was stabilized in the late Paleoproterozoic following collision of the Eastern and the Western Blocks (Zhao et al., 1999) along the Trans-North China Orogen. After this, the NCC was magmatically and tectonically quiescent until the eruption of the Fuxian and Mengyin kimberlites in the middle Ordovician (Lu et al., 1998). Late Ordovician to middle Carboniferous sedimentary rocks are absent, indicating uplift and erosion of the craton during this period. In early Mesozoic time, subduction and collision of the Yangtze Craton formed the Qinling–Dabie–Sulu Orogen along the southern margin of the NCC. Since late Mesozoic time the region has been tectonically reactivated, as evidenced by widespread intra-plate volcanism and the development of large sedimentary basins (Ren et al., 2002), both of which reflect the lithospheric modification discussed here.

The NCC is divided into two parts by a North–South Gravity Line (NSGL) running approximately parallel to, and about 400 km west of, the translithospheric Tan-Lu fault zone, a major wrench fault system that cuts through the eastern part of the NCC (Xu et al., 1987) and extends deep into the subcontinental lithospheric mantle (SCLM). East of the NSGL, the craton is characterized by a thin crust and lithosphere, high heat flow and weak negative to positive regional Bouguer anomalies. West of the NSGL, the craton is characterized by thick crust and lithosphere, low heat flow and strong negative Bouguer gravity anomalies (Yuan, 1996).

Basalts with peridotitic xenoliths occur at Jianguo village, about 30 km northeast of Fuxin City in Liaoning Province. They are alkali basalts with whole-rock K–Ar ages of ~100 Ma (Xu et al., 1999; Wang et al., 2002; Zhang and Zheng, 2003). Peridotite xenoliths are angular and small (2–2.5 cm across). The microstructural terms used to describe the peridotites in this work are after Harte (1977). The modal mineralogy of the peridotites was determined by counting more than 1000 points in each section (Table 1) and the rocks were classified using the IUGS scheme (Le Maitre, 1982). These xenoliths are dominantly porphyroclastic lherzolites with minor coarse-grained harzburgites (JG23 and JG32) and dunite (JG15). No datable sulfide was found in our collections (more than 40 samples).

The peridotitic xenoliths from the Hebi basalts (4 Ma) are highly refractory harzburgite and Cpx-poor lherzolite (high-Mg group) with minor transitional and fertile samples (low-Mg group). The high-Mg group has been interpreted as shallow relics of the Archean cratonic mantle, and the low-Mg group as newly accreted lithosphere (Zheng et al., 2001). Samples Hb028 and Hb003 from the locality are harzburgite with coarse-grained and porphyroclastic microstructures, respectively. Three-phase inclusions containing sulfides, silicates and their intergrowths (Fig. 2a), and two-phase inclusions of sulfide and silicate (Fig. 2b), were found in samples Hb028 (olivine $Mg^{\#} = 92.8$) and Hb003 (olivine $Mg^{\#} = 92.2$), respectively.

Among the well-studied peridotitic suites from eastern North China Craton (Fig. 1), the Shanwang and Nushan

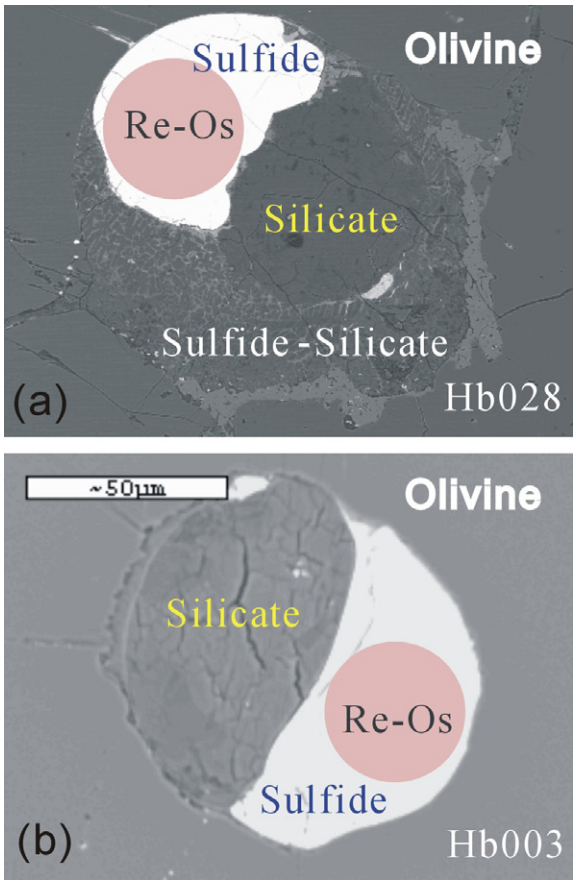

Fig. 2. Back-scattered electron images of multi-phase inclusions in the Hebi peridotites. Circles show location of Re–Os analyses.

xenoliths are associated with the deep translithospheric Tan-Lu faults (grouped as TLFZ). The SCLM beneath this area is dominantly fertile in character (Xu et al., 1998; Zheng et al., 2005a, 2006a) and has been interpreted as material that replaced the older lithosphere through extension, thermal erosion and melt-related metasomatism along the faults in Phanerozoic time (Zheng et al., 1998). The Hebi locality is located near the Gravity Gradient Zone (NSGL), but away from any active fault. The refractory mantle beneath this area has been interpreted as a shallow relic of Archean lithosphere (Zheng et al., 2001, 2005a). These two regions can serve as "end members" on a regional scale for geochemical comparisons with the Fuxin mantle peridotites and other suites.

3. ANALYTICAL METHODS

3.1. Major elements of silicates

Major-element analyses of minerals were carried out at Macquarie University on a Cameca SX50 electron microprobe (EMP), fitted with five crystal spectrometers, using an accelerating voltage of 15 kV and a sample current of 20 nA. The width of the electron beam was 5 μm. Standards were natural minerals and matrix corrections were done after the method of Pouchou and Pichoir (1984). Counting

Table 2
Electron microprobe analyses (wt%) of minerals from the Fuxin peridotite xenoliths

Type:	Type 1																													
Sample:	JG6				JG17				JG18				JG19						JG20				JG26				JG27			
Rock:	Spinel lherzolite				Spinel lherzolite				Spinel lherzolite				Spinel lherzolite						Spinel lherzolite				Spinel lherzolite				Spinel lherzolite			
Mineral:	Ol	Opx	Cpx	Sp	Ol	Opx	Cpx	Sp	Ol	Opx	Cpx	Sp	Ol	Ol	Opx	Cpx	Cpx	Sp	Ol	Opx	Cpx	Sp	Ol	Opx	Cpx	Sp	Ol	Opx	Cpx	Sp
Points:	5	5	5	5	5	5	5	5	5	5	5	5	Core	Rim	5	core	rim	5	5	5	5	5	5	5	5	5	5	5	5	5
SiO_2	40.9	55.9	52.1	0.05	41.1	56.1	54.1	0.07	40.7	55.9	51.9	0.02	40.0	39.5	55.1	52.3	52.0	0.18	40.3	55.5	52.4	0.06	40.2	55.9	52.2	0.13	40.8	55.4	52.6	0.06
TiO_2	0.01	0.07	0.22	0.14	0.01	0.18	0.43	0.36	0.03	0.07	0.32	0.44	0.01	0.02	0.07	0.27	0.34	0.14	0.01	0.07	0.28	0.13	0.00	0.08	0.17	0.11	0.00	0.09	0.18	0.18
Al_2O_3	0.00	3.31	4.41	43.4	0.01	2.84	0.84	37.3	0.04	3.07	4.67	38.7	0.02	0.02	3.97	3.29	5.52	49.4	0.02	3.10	4.27	52.9	0.04	3.25	4.21	42.3	0.02	3.29	4.63	41.6
Cr_2O_3	0.04	0.68	1.01	23.3	0.02	0.49	0.84	29.3	0.02	0.41	1.05	24.1	0.01	0.02	0.48	0.92	1.04	17.2	0.00	0.55	0.95	13.6	0.50	0.63	0.94	25.2	0.00	0.50	1.17	24.8
FeO	9.21	5.89	2.93	16.1	9.40	5.96	4.00	15.4	9.55	6.06	2.93	19.6	9.69	12.8	6.35	2.93	3.03	12.3	9.46	6.23	3.04	11.8	9.26	5.86	2.77	13.1	9.24	6.15	2.72	13.2
MnO	0.13	0.13	0.01	0.00	0.15	0.13	0.08	0.00	0.26	0.14	0.08	0.00	0.14	0.24	0.16	0.08	0.07	0.00	0.16	0.12	0.08	0.00	0.11	0.17	0.08	0.00	0.14	0.15	0.02	0.00
MgO	50.1	33.5	15.8	16.9	49.3	33.9	18.8	17.4	49.7	33.6	16.0	15.6	49.6	46.8	33.2	16.6	15.9	19.8	49.6	33.4	16.1	20.2	49.3	33.7	16.0	18.4	49.4	33.6	16.2	18.2
CaO	0.07	0.80	21.6	0.01	0.06	0.79	20.2	0.00	0.07	0.97	21.6	0.03	0.12	0.21	0.85	23.0	20.8	0.05	0.09	0.87	21.6	0.01	0.13	0.86	21.7	0.01	0.11	1.00	21.16	0.00
Na_2O	0.00	0.07	1.01	0.00	0.00	0.06	0.61	0.02	0.00	0.08	1.02	0.02	0.02	0.01	0.09	0.41	1.27	0.02	0.00	0.07	1.00	0.02	0.00	0.09	1.02	0.00	0.00	0.10	1.12	0.01
K_2O	0.00	0.00	0.00	0.00	0.02	0.01	0.03	0.00	0.01	0.00	0.00	0.02	0.00	0.00	0.01	0.00	0.00	0.00	0.00	0.01	0.01	0.02	0.01	0.01	0.02	0.00	0.00	0.01	0.00	0.03
NiO	0.27	0.10	0.00	0.29	0.47	0.12	0.02	0.22	0.47	0.00	0.00	0.29	0.48	0.30	0.16	0.00	0.12	0.42	0.39	0.13	0.02	0.35	0.44	0.11	0.03	0.33	0.40	0.11	0.10	0.21
Total	100.8	100.5	99.0	100.2	100.5	100.6	100.0	100.1	100.9	100.3	99.5	98.8	100.1	99.9	100.4	99.8	100.0	99.5	100.0	100.1	99.8	99.1	100.0	100.6	99.2	99.6	100.1	100.4	100.0	98.2
[O] =	4	6	6	4	4	6	6	4	4	6	6	4	4	4	6	6	6	4	4	6	6	4	4	6	6	4	4	6	6	4
Si	0.993	1.922	1.910	0.001	1.002	1.926	1.967	0.002	0.992	1.924	1.896	0.001	0.984	0.986	1.900	1.912	1.887	0.005	0.989	1.920	1.910	0.002	0.987	1.918	1.913	0.004	0.997	1.910	1.909	0.002
Al	0.000	0.134	0.191	1.425	0.000	0.115	0.036	1.253	0.001	0.125	0.201	1.325	0.000	0.001	0.161	0.142	0.236	1.570	0.001	0.126	0.183	1.661	0.001	0.131	0.182	1.388	0.000	0.134	0.198	1.385
Ti	0.000	0.002	0.006	0.003	0.000	0.005	0.012	0.008	0.001	0.002	0.009	0.010	0.000	0.000	0.002	0.008	0.009	0.003	0.000	0.002	0.008	0.003	0.000	0.002	0.005	0.002	0.000	0.002	0.005	0.004
Cr	0.001	0.018	0.029	0.514	0.000	0.013	0.024	0.661	0.000	0.011	0.030	0.554	0.000	0.000	0.013	0.027	0.030	0.366	0.000	0.015	0.027	0.286	0.010	0.017	0.027	0.555	0.000	0.014	0.034	0.553
Fe	0.187	0.169	0.090	0.376	0.192	0.171	0.122	0.366	0.194	0.175	0.089	0.476	0.199	0.267	0.183	0.090	0.092	0.278	0.194	0.180	0.093	0.262	0.190	0.168	0.085	0.305	0.189	0.177	0.083	0.311
Mn	0.003	0.004	0.000	0.000	0.003	0.004	0.002	0.000	0.005	0.004	0.002	0.000	0.003	0.005	0.005	0.003	0.002	0.000	0.003	0.003	0.002	0.000	0.002	0.005	0.002	0.000	0.003	0.004	0.001	0.000
Mg	1.815	1.717	0.863	0.701	1.790	1.736	1.021	0.738	1.803	1.727	0.871	0.675	1.815	1.741	1.708	0.903	0.860	0.793	1.813	1.722	0.875	0.801	1.806	1.725	0.874	0.761	1.802	1.730	0.878	0.766
Ca	0.002	0.029	0.850	0.000	0.002	0.029	0.785	0.000	0.002	0.036	0.844	0.001	0.003	0.006	0.031	0.899	0.807	0.001	0.002	0.032	0.842	0.000	0.003	0.032	0.852	0.000	0.003	0.037	0.822	0.000
Na	0.000	0.005	0.072	0.000	0.000	0.004	0.043	0.001	0.000	0.005	0.072	0.001	0.001	0.001	0.006	0.029	0.090	0.001	0.000	0.005	0.071	0.001	0.000	0.006	0.072	0.000	0.000	0.007	0.079	0.000
K	0.000	0.000	0.000	0.000	0.001	0.000	0.001	0.000	0.000	0.000	0.000	0.001	0.000	0.000	0.000	0.000	0.000	0.000	0.000	0.000	0.001	0.001	0.000	0.000	0.001	0.000	0.000	0.000	0.000	0.001
Ni	0.005	0.003	0.000	0.006	0.009	0.003	0.000	0.005	0.009	0.000	0.000	0.007	0.009	0.006	0.004	0.000	0.003	0.009	0.008	0.004	0.000	0.008	0.009	0.003	0.001	0.007	0.008	0.003	0.003	0.005
Sum	3.01	4.00	4.01	3.03	3.00	4.01	4.01	3.03	3.01	4.01	4.02	3.05	3.02	3.01	4.01	4.01	4.02	3.03	3.01	4.01	4.01	3.02	3.01	4.01	4.01	3.02	3.00	4.02	4.01	3.03
$Mg^{\#}$	90.7	91.0	90.6	65.1	90.3	91.0	89.4	66.9	90.3	90.8	90.7	58.6	90.1	86.7	90.3	91.0	90.4	74.1	90.3	90.5	90.4	75.3	90.5	91.1	91.2	71.4	90.5	90.7	91.4	71.1
$Cr^{\#}$			13.3	26.5			40.1	34.5			13.1	29.5				15.8	11.2	18.9			13.0	14.7			13.1	28.5			14.5	28.5

(*continued on next page*)

Table 2 (*continued*)

Type:	Type 1											Type 2						Type 3												
Sample:	JG28					JG29				JG15		JG23			JG32			JG10				JG12			JG13-1				JG13-2		
Rock:	Spinel lherzolite					Spinel lherzolite				Spinel dunite		Spinel harzburgite			Spinel harzburgite			Spinel lherzolite				Lherzolite			Spinel lherzolite				Spinel lherzolite		
Mineral:	Ol	Opx	Cpx	Cpx	Sp	Ol	Opx	Cpx	Sp	Ol	Sp	Ol	Opx	Sp	Ol	Opx	Sp	Ol	Opx	Cpx	Sp	Ol	Opx	Cpx	Ol	Opx	Cpx	Sp	Ol	Opx	Cpx
Points:	5	5	Core	Rim	5	5	5	5	5	5	5	5	5	5	5	5	5	5	5	5	5	5	5	5	5	5	5	5	5	5	5
SiO_2	41.0	55.3	52.8	52.7	0.07	40.6	55.2	52.0	0.0	40.5	0.18	41.2	57.4	0.85	40.9	57.1	0.17	39.9	55.0	52.4	0.10	39.4	55.0	52.0	39.9	54.9	52.1	0.04	40.1	54.9	52.4
TiO_2	0.00	0.09	0.16	0.22	0.14	0.00	0.04	0.25	0.08	0.04	0.47	0.02	0.06	0.40	0.00	0.06	0.41	0.01	0.11	0.23	0.32	0.00	0.11	0.19	0.03	0.08	0.10	0.28	0.00	0.08	0.28
Al_2O_3	0.04	3.22	2.57	4.61	41.2	0.00	4.01	5.17	53.4	0.01	26.3	0.00	1.67	21.6	0.01	1.67	21.5	0.02	2.43	3.50	31.2	0.06	2.98	4.51	0.02	2.62	3.73	31.1	0.02	2.93	4.00
Cr_2O_3	0.03	0.57	1.42	1.04	25.6	0.00	0.37	0.79	13.7	0.02	38.9	0.02	0.50	45.7	0.02	0.50	45.6	0.01	0.42	0.78	29.7	0.03	0.50	1.29	0.03	0.42	0.85	29.4	0.02	0.16	0.31
FeO	9.44	6.07	2.48	3.14	13.8	9.54	6.33	2.78	12.1	10.8	19.2	7.63	4.86	13.9	7.79	5.18	14.6	12.8	8.46	3.88	23.0	14.7	8.85	3.17	13.3	8.94	4.43	23.4	13.1	8.34	4.22
MnO	0.19	0.13	0.03	0.11	0.00	0.11	0.14	0.14	0.00	0.09	0.00	0.13	0.14	0.00	0.10	0.03	0.00	0.26	0.17	0.07	0.00	0.22	0.26	0.09	0.14	0.17	0.11	0.00	0.17	0.19	0.06
MgO	49.6	33.5	16.9	16.6	18.2	49.5	33.7	16.0	20.5	48.5	15.1	50.7	35.1	15.6	50.8	35.2	15.6	46.0	31.8	16.1	14.2	44.7	31.4	15.8	45.8	32.0	15.5	13.9	46.8	32.2	16.1
CaO	0.12	0.93	23.1	20.9	0.00	0.09	0.83	21.9	0.00	0.09	0.03	0.05	0.82	0.14	0.02	0.79	0.03	0.09	0.85	21.1	0.03	0.13	0.85	21.1	0.06	0.75	21.2	0.02	0.08	0.88	21.3
Na_2O	0.03	0.09	0.49	1.16	0.00	0.01	0.04	0.92	0.02	0.02	0.01	0.00	0.07	0.02	0.01	0.05	0.02	0.00	0.06	1.02	0.00	0.01	0.09	1.26	0.00	0.05	1.03	0.02	0.01	0.05	0.92
K_2O	0.03	0.00	0.02	0.00	0.02	0.00	0.00	0.01	0.01	0.00	0.00	0.00	0.02	0.00	0.02	0.00	0.01	0.02	0.01	0.00	0.00	0.00	0.02	0.00	0.00	0.01	0.01	0.00	0.00	0.02	0.00
NiO	0.43	0.10	0.06	0.04	0.36	0.50	0.11	0.08	0.29	0.67	0.28	0.69	0.06	0.20	0.40	0.08	0.32	0.27	0.05	0.05	0.27	0.30	0.08	0.02	0.40	0.12	0.00	0.25	0.19	0.09	0.03
Total	100.9	100.0	100.0	100.5	99.4	100.4	100.8	99.9	100.1	100.7	100.4	100.4	100.7	98.5	100.1	100.7	98.2	99.5	99.3	99.2	98.9	99.6	100.2	99.4	99.7	100.1	99.0	98.5	100.5	99.8	99.5
[O] =	4	6	6	6	4	4	6	6	4	4	4	4	6	4	4	6	4	4	6	6	4	4	6	6	4	6	6	4	4	6	6
Si	0.996	1.914	1.925	1.902	0.002	0.992	1.897	1.889	0.001	0.993	0.005	0.998	1.958	0.026	0.995	1.951	0.005	0.999	1.934	1.927	0.003	0.995	1.924	1.903	0.999	1.922	1.923	0.001	0.994	1.921	1.918
Al	0.001	0.131	0.110	0.196	1.363	0.000	0.162	0.221	1.658	0.000	0.936	0.000	0.067	0.783	0.000	0.067	0.786	0.001	0.101	0.152	1.117	0.002	0.123	0.195	0.000	0.108	0.162	1.120	0.001	0.121	0.173
Ti	0.000	0.002	0.004	0.006	0.003	0.000	0.001	0.007	0.001	0.001	0.011	0.000	0.002	0.009	0.000	0.002	0.009	0.000	0.003	0.006	0.007	0.000	0.003	0.005	0.001	0.002	0.003	0.006	0.000	0.002	0.008
Cr	0.001	0.016	0.041	0.030	0.568	0.000	0.010	0.023	0.286	0.000	0.929	0.000	0.013	1.113	0.000	0.013	1.121	0.000	0.012	0.023	0.713	0.000	0.014	0.037	0.001	0.012	0.025	0.710	0.000	0.004	0.009
Fe	0.192	0.176	0.076	0.095	0.324	0.195	0.182	0.084	0.267	0.222	0.484	0.155	0.138	0.359	0.158	0.148	0.380	0.268	0.249	0.119	0.585	0.311	0.259	0.097	0.279	0.262	0.137	0.599	0.272	0.244	0.129
Mn	0.004	0.004	0.001	0.003	0.000	0.002	0.004	0.004	0.000	0.002	0.000	0.003	0.004	0.000	0.002	0.001	0.000	0.006	0.005	0.002	0.000	0.005	0.008	0.003	0.003	0.005	0.003	0.000	0.004	0.005	0.002
Mg	1.798	1.728	0.918	0.894	0.762	1.805	1.723	0.867	0.805	1.771	0.679	1.830	1.784	0.716	1.839	1.793	0.720	1.717	1.668	0.881	0.641	1.682	1.637	0.861	1.708	1.671	0.853	0.634	1.729	1.680	0.877
Ca	0.003	0.035	0.901	0.810	0.000	0.002	0.031	0.851	0.000	0.002	0.001	0.001	0.030	0.005	0.000	0.029	0.001	0.002	0.032	0.832	0.001	0.003	0.032	0.829	0.002	0.028	0.838	0.001	0.002	0.033	0.835
Na	0.001	0.006	0.035	0.081	0.000	0.001	0.003	0.065	0.001	0.001	0.000	0.000	0.005	0.001	0.001	0.004	0.001	0.000	0.004	0.073	0.000	0.000	0.006	0.089	0.000	0.003	0.074	0.001	0.000	0.003	0.065
K	0.001	0.000	0.001	0.000	0.001	0.000	0.000	0.000	0.000	0.000	0.000	0.000	0.001	0.000	0.001	0.000	0.000	0.001	0.001	0.000	0.000	0.000	0.001	0.000	0.000	0.000	0.000	0.000	0.000	0.001	0.000
Ni	0.008	0.003	0.002	0.001	0.008	0.010	0.003	0.002	0.006	0.013	0.007	0.013	0.002	0.005	0.008	0.002	0.008	0.005	0.001	0.002	0.007	0.006	0.002	0.001	0.008	0.003	0.000	0.006	0.004	0.002	0.001
Sum	3.00	4.014	4.01	4.02	3.03	3.01	4.02	4.01	3.03	3.01	3.05	3.00	4.00	3.02	3.01	4.01	3.03	3.00	4.01	4.02	3.07	3.00	4.01	4.02	3.00	4.02	4.02	3.08	3.01	4.02	4.02
$Mg^{\#}$	90.4	90.8	92.4	90.4	70.2	90.2	90.5	91.1	75.1	88.9	58.4	92.2	92.8	66.6	92.1	92.4	65.5	86.5	87.0	88.1	52.3	84.4	86.3	89.9	86.0	86.5	86.2	51.4	86.4	87.3	87.2
$Cr^{\#}$			27.1	13.1	29.4			9.3	14.7		49.8			58.7			58.8			13.0	39.0			16.1			13.2	38.8			5.0

$Mg^{\#} = Mg/(Mg + Fe)$ and $Cr^{\#} = Cr/(Cr + Al)$.

Table 3
Trace element concentrations of olivine in the Fuxin peridotite xenoliths (ppm)

Type	Type 1										Type 2		Type 3			Hebi ($n = 9$)[a] average (range)	TLFZ ($n = 15$)[a] average (range)
Sample	JG6	JG17	JG18	JG19	JG20	JG26	JG27	JG28	JG29	JG15	JG23	JG32	JG10	JG13-1	JG13-2		
Ca	433	380	552	604	603	490	624	749	455	427	301	337	426	390	557	1034 (806–1284)	546 (381–957)
Sc	2.62	1.66	2.41	2.12	1.84	2.66	2.96	2.31	1.82	1.52	1.63	1.76	2.80	1.44	2.26	4.18 (3.45–4.58)	3.29 (2.60–4.80)
Ti	27.0	20.1	14.4	17.2	21.5	8.42	10.7	11.2	7.58	14.3	14.6	17.1	38.1	6.66	20.9	12.8 (2.60–26.4)	16.6 (13.0–20.2)
V	10.8	1.94	4.49	3.12	3.06	2.81	3.26	3.00	2.34	1.68	1.47	1.65	6.20	1.66	3.39	2.74 (1.61–3.61)	2.09 (1.78–2.83)
Cr	445	100	362	100	98.3	102	145	125	62.1	96.5	178	237	236	970	33.4	176 (91.6–254)	47.5 (32.2–78.8)
Mn	1050	892	963	968	941	871	926	927	959	929	666	699	1467	1173	1189	788 (724–915)	913 (771–1001)
Co	151	142	148	138	146	128	136	138	139	159	151	149	158	165	186	171 (161–183)	110 (94.2–127)
Ni	3040	2923	2903	2847	3010	2725	2872	3029	2919	2520	3824	3839	2301	2319	1691	3785 (3450–4088)	1372 (1997–2610)
Zn	67.9	74.9	80.2	60.6	65.6	49.3	56.5	62.3	69.7	112	73.8	79.0	116	120	84.0	43.1 (37.4–58.7)	35.6 (26.2–50.8)

[a] Zheng et al. (2006a).

Table 4
Trace element concentrations of orthopyroxene in the Fuxin peridotite xenoliths (ppm)

Type	Type 1									Type 2		Type 3			Hebi ($n = 5$)[a]	TLFZ ($n = 9$)[a]
Sample	JG6	JG17	JG18	JG19	JG20	JG26	JG27	JG28	JG29	JG23	JG32	JG10	JG13-1	JG13-2		
Ca	4491	4570	4680	5259	6800	5557	5992	5558	4525	5130	5278	4640	4860	4890	6113 (5300–6738)	4330 (3594–5742)
Sc	17.9	10.5	14.4	16.2	15.7	16.8	19.5	16.1	14.7	9.19	8.76	14.1	10.3	9.82	15.7 (12.0–19.2)	16.4 (13.5–21.1)
Ti	425	895	480	553	459	319	401	363	368	510	511	351	276	213	163 (7.64–468)	596 (441–786)
V	141	54.1	81.9	95.8	90.1	81.2	113	86.5	85.9	40.6	42.1	69.3	40.8	40.9	51.4 (41.9–57.9)	66.8 (58.4–85.7)
Cr	5519	2322	2811	3153	3139	2923	4232	3600	2248	3109	3280	2405	2628	2911	3981 (2420–4510)	1781 (1333–2044)
Mn	977	913	994	966	988	874	989	975	973	726	733	1148	1324	1253	808 (761–920)	914 (826–1076)
Co	59.4	55.6	62.1	58.7	63.7	49.8	58.9	59.5	56.6	61.2	62.2	61.4	73.0	70.9	47.3 (46.6–50.6)	45.3 (38.9–55.2)
Ni	910	695	768	745	840	640	772	816	742	967	986	575	640	622	987 (933–1014)	530 (491–687)
Zn	47.9	46.8	60.5	38.7	49.4	29.3	36.9	48.6	47.1	60.5	55.9	66.3	97.6	95.8	26.8 (24.3–34.5)	23.7 (16.2–34.8)
Ga	4.22	4.12	3.96	3.15	4.23	2.70	3.31	2.82	3.68	2.82	2.64	3.17	4.68	4.69	3.78 (1.78–8.30)	4.74 (3.08–7.10)
Y	0.90	0.62	0.48	0.82	0.59	0.66	0.94	0.47	0.74	0.53	0.50	0.46	0.49	0.55	0.22 (0.05–0.55)	0.97 (0.67–1.18)
Zr	1.16	1.45	1.19	1.17	1.57	2.28	1.17	0.59	1.63	0.76	0.90	2.43	2.03	3.44	1.20 (0.20–3.71)	1.45 (0.61–2.05)

[a] Zheng et al. (2006a).

times were 10 s for peaks and 5 s for background on either side of the peak. Major-element abundances of rock-forming minerals reported in Table 2 generally represent averages of more than 5-point analyses of each grain and several grains from different parts of each sample. In order to examine whether equilibrium had been attained, considerable attention was paid to determining the homogeneity of individual phases. All of the minerals from the Fuxin peridotites (except JG19 and JG28) are homogeneous within 2 standard errors of the mean. JG19 and JG28 show some heterogeneity in olivine and clinopyroxene compositions.

3.2. Trace elements of silicates

Trace-element analyses of minerals were carried out at Macquarie University using a 266-nm UV LASER ablation microprobe coupled to an ICPMS (LAM-ICPMS). The LASER ablation system is similar to the one described by Norman et al. (1996). The laser is a Continuum Surelite I-20 Q-switched and frequency quadrupled Nd:YAG LASER with a fundamental infrared (IR) wavelength at 1064 nm, quadrupled to 266 nm, and a pulse width of 5–7 ns. Most analyses are done with beam energy in the range of 0.5–3 mJ/pulse. The ICPMS is an Agilent 7500. The NIST 610 and 612 glasses were used as external standards; internal standards were Ca for clinopyroxene, and Mg for olivine, orthopyroxene and spinel. BCR-1 and an in-house reference garnet were run as unknowns in each sample batch to check accuracy. Data were reduced using the in-house GLITTER on-line software (van Achterbergh et al., 2001). Trace-element abundances of olivine (Table 3), orthopyroxene (Table 4) and clinopyroxene (Table 5) represent averages of five points of analysis for each phase.

3.3. In-situ Re–Os dating of sulfide

Backscattered electron (BSE) images and compositions of sulfides (Fig. 2) were acquired using a CAMEBAX SX50 electron microprobe at the GEMOC ARC National

Table 5
Trace element concentrations of clinopyroxene (ppm) in the Fuxin peridotite xenoliths

Type	Type 1									Type 3		
Sample	JG6	JG17	JG18	JG19	JG20	JG26	JG27	JG28	JG29	JG10	JG13-1	JG13-2
Points	5	5	5	5	5	5	5	5	5	5	5	5
P	23.6	227	37.1	45.4	71.1	61.0	35.1	27.7	26.1	56.6	66.1	61.4
Sc	55.3	38.7	66.8	60.5	58.9	65.3	63.3	60.7	52.2	58.7	41.9	54.3
Ti	1222	6546	1646	1968	1555	1587	1089	1061	1533	1151	683	1330
V	223	199	244	241	286	226	224	209	211	212	139	209
Cr	6536	4333	6349	5839	7291	6005	7266	7124	4173	5976	5185	1948
Mn	666	3444	589	561	676	554	587	543	607	686	714	637
Co	22.0	166	21.0	18.7	26.9	18.1	21.0	19.0	18.4	23.9	24.4	22.5
Ni	331	1227	325	308	413	327	364	370	276	283	279	158
Zn	16.6	200	15.5	12.1	25.1	12.6	13.9	13.1	14.1	20.7	29.5	15.1
Ga	3.69	18.0	4.48	3.41	6.14	5.83	3.17	2.84	3.33	3.74	5.81	3.78
Rb	0.05	7.68	b.d.	0.18	0.99	0.56	0.35	b.d.	b.d.	b.d.	0.26	b.d.
Sr	112	119	112	91.4	111	146	49.9	51.0	101	161	206	145
Y	6.36	13.3	8.73	11.8	7.28	9.22	6.98	6.47	10.2	5.54	8.03	5.89
Zr	12.3	67.2	24.5	17.1	20.1	46.7	7.80	7.16	18.6	34.7	44.4	10.0
Nb	0.05	11.2	0.03	0.22	0.11	2.71	0.18	0.13	0.03	0.20	0.04	0.09
Ba	0.29	41.2	b.d.	0.72	5.50	24.4	0.80	0.16	0.36	0.37	1.71	0.09
La	1.98	6.90	2.14	2.66	2.02	5.16	1.07	1.01	2.27	3.80	6.41	4.33
Ce	6.63	21.5	8.47	10.1	10.7	16.3	3.34	3.25	7.66	12.2	22.1	13.7
Pr	1.04	3.27	1.60	1.94	1.67	2.52	0.59	0.58	1.26	1.93	3.17	1.98
Nd	4.95	15.5	8.32	10.1	8.71	11.7	2.98	2.86	5.97	8.33	13.4	8.46
Sm	1.29	3.94	2.76	2.83	2.50	2.98	0.84	0.80	1.72	1.99	2.63	1.74
Eu	0.46	1.42	0.76	0.88	0.88	0.79	0.28	0.28	0.61	0.59	0.83	0.55
Gd	1.18	3.45	2.65	2.77	2.15	2.43	1.05	0.92	1.81	1.52	1.98	1.43
Tb	0.19	0.50	0.36	0.40	0.30	0.32	0.17	0.16	0.31	0.22	0.28	0.20
Dy	1.24	3.01	2.05	2.53	1.78	2.04	1.24	1.14	2.00	1.38	1.70	1.28
Ho	0.25	0.56	0.39	0.48	0.35	0.39	0.27	0.26	0.42	0.29	0.31	0.24
Er	0.67	1.44	1.05	1.33	0.97	0.91	0.79	0.73	1.18	0.84	0.84	0.57
Tm	0.09	0.19	0.12	0.22	0.18	0.13	0.11	0.11	0.17	0.13	0.11	0.07
Yb	0.61	1.11	0.76	1.27	1.20	0.90	0.73	0.76	1.10	0.89	0.76	0.53
Lu	0.08	0.18	0.15	0.20	0.15	0.11	0.11	0.10	0.16	0.15	0.09	0.07
Hf	0.48	1.73	1.37	0.70	1.40	0.93	0.27	0.26	0.79	1.03	1.18	0.40
Ta	b.d.	0.41	0.06	0.04	b.d.	0.14	b.d.	b.d.	0.06	0.08	b.d.	0.02
Pb	0.54	0.48	0.52	0.64	1.26	0.34	0.21	0.21	0.32	0.55	0.50	0.18
Th	0.16	0.49	0.32	0.26	0.27	0.49	0.06	0.10	0.24	0.64	0.31	0.18
U	0.04	0.21	0.29	0.17	0.15	0.14	0.02	b.d.	0.08	0.25	0.04	0.03

b.d., below the detect limit.

Key Centre, Macquarie University, Australia. Natural minerals and synthetic were used as standards. Analytical conditions included an accelerating voltage of 15 keV, a beam current of 20-nA, beam size of 5 μm and counting time of 20 s for all elements. All analyses underwent a full ZAF correction.

Re–Os isotope data listed in Table 6 were obtained using Merchantek LUV266 LASER microprobe with a modified ablation cell, attached to the Nu plasma MC-ICPMS at GEMOC Key Centre (www.es.mq.edu/GEMOC/). All ablations were carried out using He as the carrier gas. Most analyses were done at 4 Hz repetition rate and energies of ca. 2 mJ/pulse; typical pit diameters were 50-80 μm. The analytical procedures have been described in detail by Pearson et al. (2002). A dry aerosol of Ir, produced by a CETAC MCN6000 desolvating nebulizer, was bled into the gas line between the ablation cell and the ICPMS to provide a massbias correction with a precision independent of the abundance of Os in the sample. The total Ir signal is typically 2–3 V. Pearson et al. (2002) have demonstrated that this procedure provides a significant improvement to precision relative to the use of the Os isotopes of the sample itself, especially for samples with low signals. Masses 188–194 were measured in Faraday cups, and masses 185 and 187 were measured in ETP ion counters. The measurement of ^{185}Re is used to correct for the overlap of ^{187}Re on ^{187}Os (Pearson et al., 2002). The precision and accuracy of the method are discussed in detail by Pearson et al. (2002). Under ideal circumstances (sulfides >50 μm diameter, >ca. 40 ppm Os), an internal precision for $^{187}Os/^{188}Os$ of 0.1–0.3% is routinely obtained; for smaller grains or lower Os contents (to 1–5 ppm) precision of 1–2% is routine. The external reproducibility of $^{187}Os/^{188}Os$ for the PGE-A standard over several months is ±0.0004 (2SD). The $^{187}Re/^{188}Os$ ratio is measured directly.

Both the model age (T_{MA}) and re-depletion model age (T_{RD}) were also calculated (Table 6). As applied to sulfide analysis, T_{MA} assumes that the measured Re/Os of the sample has remained unchanged since the sulfide crystallized, and may record either a melt-depletion event (residual sulfide) or a metasomatic event (secondary sulfides, assumed to be derived from the convection mantle). T_{RD} assumes that any measured Re has been introduced at a late stage, and is used to estimate the minimum age of the mantle melting event, that produced the analysed sulfide (cf. Shirey and Walker, 1998; Pearson, 1999).

4. RESULTS

4.1. Mineral chemistry

4.1.1. Olivine

The Fuxin peridotites can be subdivided into three types, based on their olivine compositions (Table 2): (1) Type 1, the dominant lherzolites with $Mg^{\#}$-olivine = 88.9–90.7; (2) Type 2, two harzburgites (JG23 and JG32) with high $Mg^{\#}$-olivine (~92.0) and (3) Type 3, four lherzolites including samples JG10, JG12, JG13-1 and JG13-2, with low $Mg^{\#}$-olivine (84.4–86.5). Olivine in JG19 is

Table 6
In situ Re–Os analysis of sulfides in the Hebi and Hannuoba peridotites

Locality	Sample/grain	Grain	State	$Mg^{\#}$ in Ol	$Cr^{\#}$ in Cpx	$^{187}Os/^{188}Os$	1σ	$^{187}Re/^{188}Os$	1σ	T_{MA} (Ga)	1σ (Ga)	T_{RD} (Ga)	1σ (Ga)
Hebi	Hb028		Enclosed	92.8	43.2	0.10651	0.00069	0.00105	0.00002	3.0	0.1	3.0	0.1
	Hb003		Enclosed	92.2	36.4	0.11024	0.00074	0.00590	0.00060	2.5	0.1	2.5	0.1
Hannuoba	JSB02-2		Enclosed	92.8	23.5	0.11240	0.00400	0.00258	0.00048	2.2	0.6	2.1	0.6
	DM02-9	DM02-9-1	Enclosed	91.2	23.7	0.11839	0.00110	0.03649	0.00260	1.4	0.2	1.3	0.2
		DM02-9-2	Interstitial			0.11744	0.00080	0.21552	0.00440	3.0	0.3	1.4	0.1
		DM02-9-3	Interstitial			0.00091	0.21225	0.00370	3.1	0.3	1.5	0.1	
	DM02-11	DM02-11-4	Enclosed	90.6	9.3	0.12192	0.00250	0.14259	0.00180	1.2	0.6	0.8	0.4
		DM02-11-5	Interstitial			0.12201	0.00110	0.06899	0.00084	0.9	0.2	0.7	0.2
		DM02-11-8	Interstitial			0.12124	0.00028	0.15554	0.00079	1.4	0.1	0.9	0.0

$Mg^{\#}$ of Ol and $Cr^{\#}$ of Cpx: Hebi, Zheng et al. (2001); Hannuoba, Yu et al. (2006).

heterogeneous, with $Mg^{\#} = 90.1$ in the cores of grains and $Mg^{\#} = 86.7$ in the rims.

There are large ranges in V (1.66–10.8 ppm) and Cr (62.1–970 ppm), but limited variation in other trace element contents (Ca, Ni, Sc, Co, Ti, Mn and Zn) in the olivines of the Fuxin peridotites (Table 3). The olivines in the high-$Mg^{\#}$ Type 2 peridotites have the highest Ni but the lowest Ca and Mn contents. Low CaO in olivine suggests a low equilibration temperature (O'Reilly et al., 1996). Fo shows positive correlation with Ni, negative correlation with Mn, and no correlation with Co and Ni/Cr (Fig. 3a–d).

The olivines in the Type 2 peridotites have similar Ni, Co and Mn to the Hebi high-$Mg^{\#}$ group xenoliths. The Ni and Co contents of the Type 1 peridotitic olivines are intermediate between those of the Hebi and TLFZ xenoliths. Those in the Type 3 samples have similar Co but low Ni compared to the Hebi suite, and much higher Mn than the Hebi and TLFZ peridotites.

4.1.2. Orthopyroxene

The $Mg^{\#}$ of orthopyroxene, as with their coexisting olivines, can be subdivided into three types: moderate-$Mg^{\#}$ (90.3–91.1) in Type 1, high-$Mg^{\#}$ (~92.5) in Type 2 and low-$Mg^{\#}$ (86.3–87.4) in Type 3.

There is large range in Cr (2322–5519 ppm), but limited variation in other trace element contents in the orthopyroxenes of the Fuxin peridotites (Table 4). The orthopyroxene in the high-$Mg^{\#}$ Type 2 peridotites contains the highest Ni (967–986 ppm) but the lowest Sc, Mn, Zr and Ga contents. In contrast, those in the low-$Mg^{\#}$ Type 3 xenoliths are the highest in Mn, Zn and Zr but the lowest in Ni, Cr and Ti contents. $Mg^{\#}$ shows positive correlations with Ni and

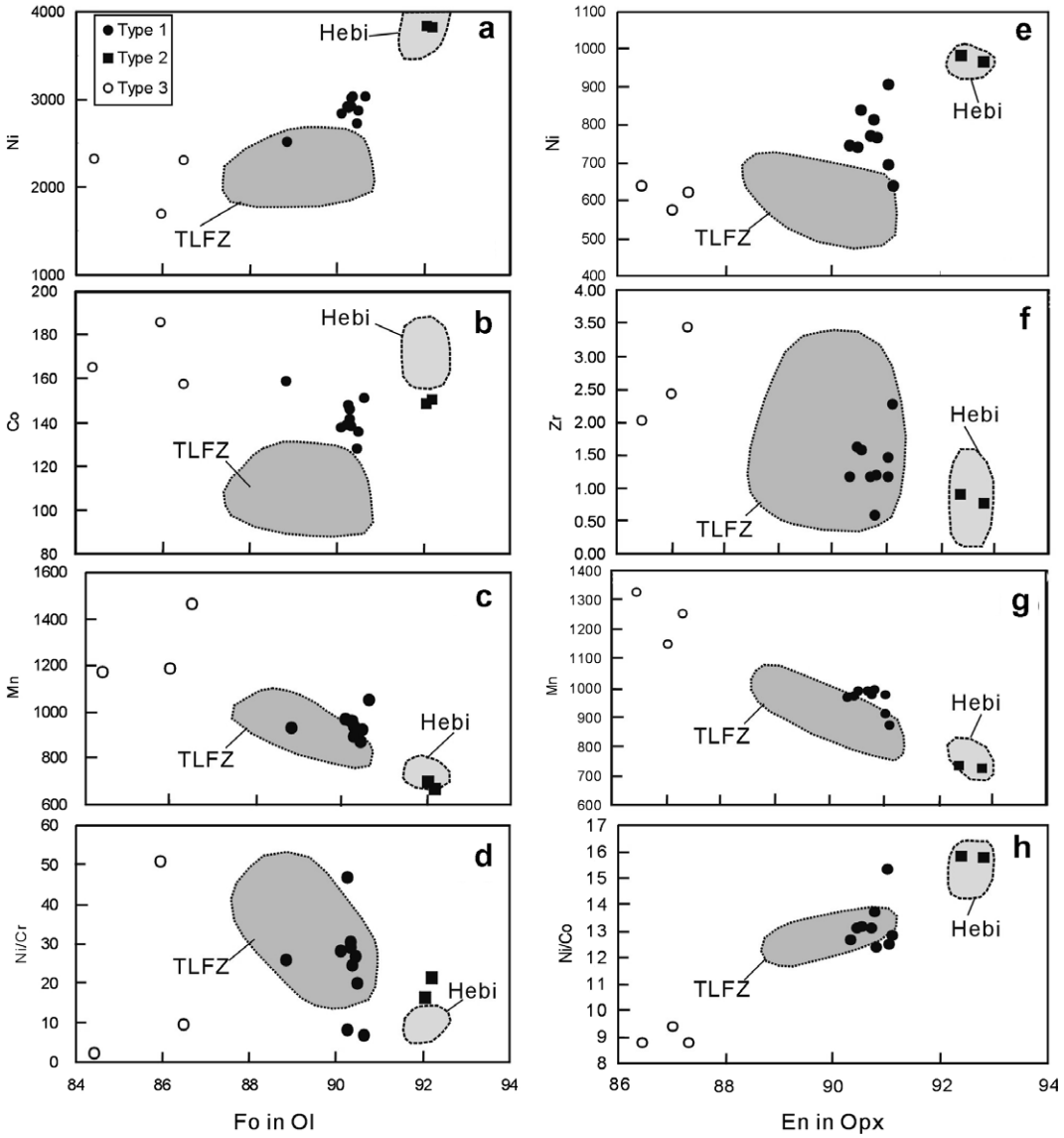

Fig. 3. Plots of %Fo in Ol (a–d) and %En in Opx (e–h) vs trace elements. Other data sources: Hebi, Zheng et al. (2001) and TLFZ (translithospheric Tan-Lu fault zone including Shanwang and Nushan), Zheng et al. (1998, 2006a) and Xu et al. (1998).

Ni/Co, and negative correlations with Mn and Zr (Fig. 3e–h).

The orthopyroxenes in the Type 2 peridotites have similar Ni, Zr, Mn and Ni/Co to the Hebi high-$Mg^{\#}$ xenoliths. In contrast, the Type 1 peridotitic opx have similar Zr, Mn and Ni/Co to those of the TLFZ xenoliths, but intermediate Ni between the Hebi and TLFZ. Those in the Type 3 samples are high in Mn but low in Ni/Co compared to the Hebi and TLFZ peridotites.

4.1.3. Clinopyroxene

The $Mg^{\#}$ and $Cr^{\#}$ of the clinopyroxenes in the Type 1 peridotites are 89.4–92.4 and 9.3–40.1, respectively. Samples JG19 and JG28 have higher $Mg^{\#}$ and $Cr^{\#}$ values in cores than in rims (Table 2). The clinopyroxenes in the Type 3 xenoliths are also high in FeO and thus have low $Mg^{\#}$. The contents of Na_2O, Al_2O_3 and Cr_2O_3 show large ranges (0.41–1.27 wt%, 0.84–4.67 wt% and 0.31–1.42 wt%, respectively). Samples JG19 and JG28 have lower Na_2O, TiO_2, FeO and Al_2O_3 contents in cores than in rims. No clinopyroxene has been found in the high-$Mg^{\#}$ Type 2 samples.

La contents of the Type 1 peridotitic clinopyroxenes are 1.0–7.0 ppm (Table 5). The chondrite normalized REE patterns of the clinopyroxene vary from flat (JG27 and JG28) to convex upward. Those in the Type 3 xenoliths have low HREE contents and thus high LREE/HREE ratios relative to the clinopyroxenes in the Type 1 xenoliths, and all show convex upward LREE patterns. Most of the Fuxin clinopyroxenes have obvious negative anomalies in Ti, Nb, Pb and Zr (Fig. 4). Samples JG16, JG19 and JG20 have positive anomalies in Ba, negative (e.g. JG20) to positive anomalies in Nb (e.g. JG117) and in Pb (e.g. JG20).

There are no obvious positive correlations between $Cr^{\#}$ and La/Yb, or negative correlations between $Cr^{\#}$ and incompatible trace elements (Fig. 5); but there are positive correlations between La and Zr and Sr, suggesting that at least two events, primary depletion and secondary enrichment, have affected the lithospheric mantle beneath the Fuxin area. The Fuxin clinopyroxenes have relatively high Ti, low La, Ce, Sr, Nb and La/Yb to those in the Hebi refractory peridotites, but overlap the ranges defined by the clinopyroxenes from the TLFZ.

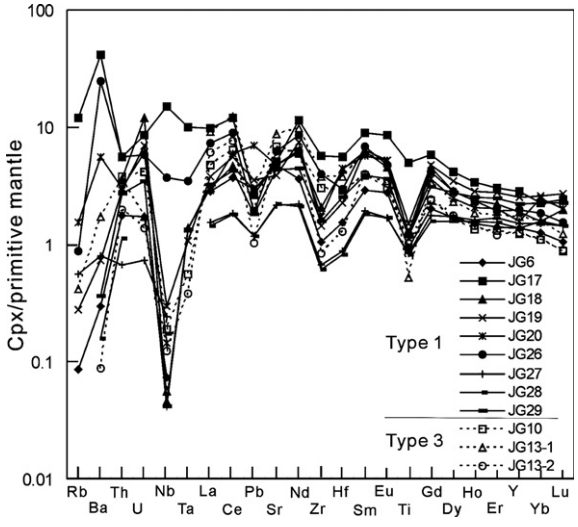

Fig. 4. Primitive mantle-normalised trace element patterns of clinopyroxenes from Fuxin xenoliths.

4.1.4. Spinel

The Cr_2O_3 contents of spinel are moderate in the lherzolites, including the Type 1 and Type 3 samples (13.6–29.3 wt%), but high (~45.6 wt%) in the harzburgites. The low $Cr^{\#}$ of spinels and low $Mg^{\#}$ of coexisting clinopyroxenes in most Fuxin samples indicate that most of the upper SCLM beneath the region has been subjected to relatively low degrees of melt extraction, especially compared to the refractory xenoliths from Hebi. However, most of them are at the higher end of the compositional range defined by samples from the TLFZ, implying higher degrees of melt extraction on average, compared to the lithospheric mantle beneath the TLFZ (Table 1). Two Type 3 lherzolites have low $Mg^{\#}$ in clinopyroxene (also in coexisting olivine and orthopyroxene) but high $Cr^{\#}$ in spinel relative to Type 1, suggesting they record the interaction of basaltic melt with the refractory peridotites.

4.2. Re–Os model ages

No datable sulfides were found in the Fuxin xenoliths. Sulfide inclusions in two Hebi peridotites give Archean T_{RD} and T_{MA} model ages, i.e. 3.0 ± 0.1 Ga in Hb028 and 2.5 ± 0.1 Ga in Hb003 (Table 6), and confirm the inference, drawn from mineral chemistry, that these samples represent relict Archean lithospheric mantle. The silicate-enclosed sulfides of two Hannuoba peridotites yield younger T_{RD} and T_{MA} model ages, i.e. Paleoproterozoic ($2.1 \sim 2.2 \pm 0.6$ Ga) in JSB02-2 and Mesoproterozoic (1.4 ± 0.2 Ga) in DM02-9-1, broadly consistent with whole-rock model ages on samples from this locality (Gao et al., 2002). The sulfides of sample DMP02-11, including both enclosed and interstitial occurrences, show T_{RD} of 0.7–0.9 Ga. Two of the sulfides from the Hannuoba xenoliths (DM02-9-2 and -3) have very large differences between T_{MA} (3.0–3.1 Ga) and T_{RD} (1.4–1.5 Ga).

4.3. Equilibration temperatures

Equilibration temperatures (T) for the Fuxin peridotites have been estimated at an assumed pressure of 1.5 GPa, using published thermometers, based on Fe–Mg partitioning between pyroxenes (Wells, 1977; Sachtleben and Seck, 1981), Ca content in orthopyroxene (Brey and Köhler, 1990) and Al exchange among olivine, orthopyroxene and spinel (Witt-Eickschen and Seck, 1991). The three kinds of thermometers give similar temperature estimates (Table 7). Estimates based on the Ca-in-Opx thermometer (Brey and Köhler, 1990) fall within the range 863-1138 °C for Type 1 and 964-977 °C for Type 3 peridotites. Samples JG19 and JG28 give higher temperature estimates for rims than for cores. The estimates for the Type 2 xenoliths fall into the same ranges.

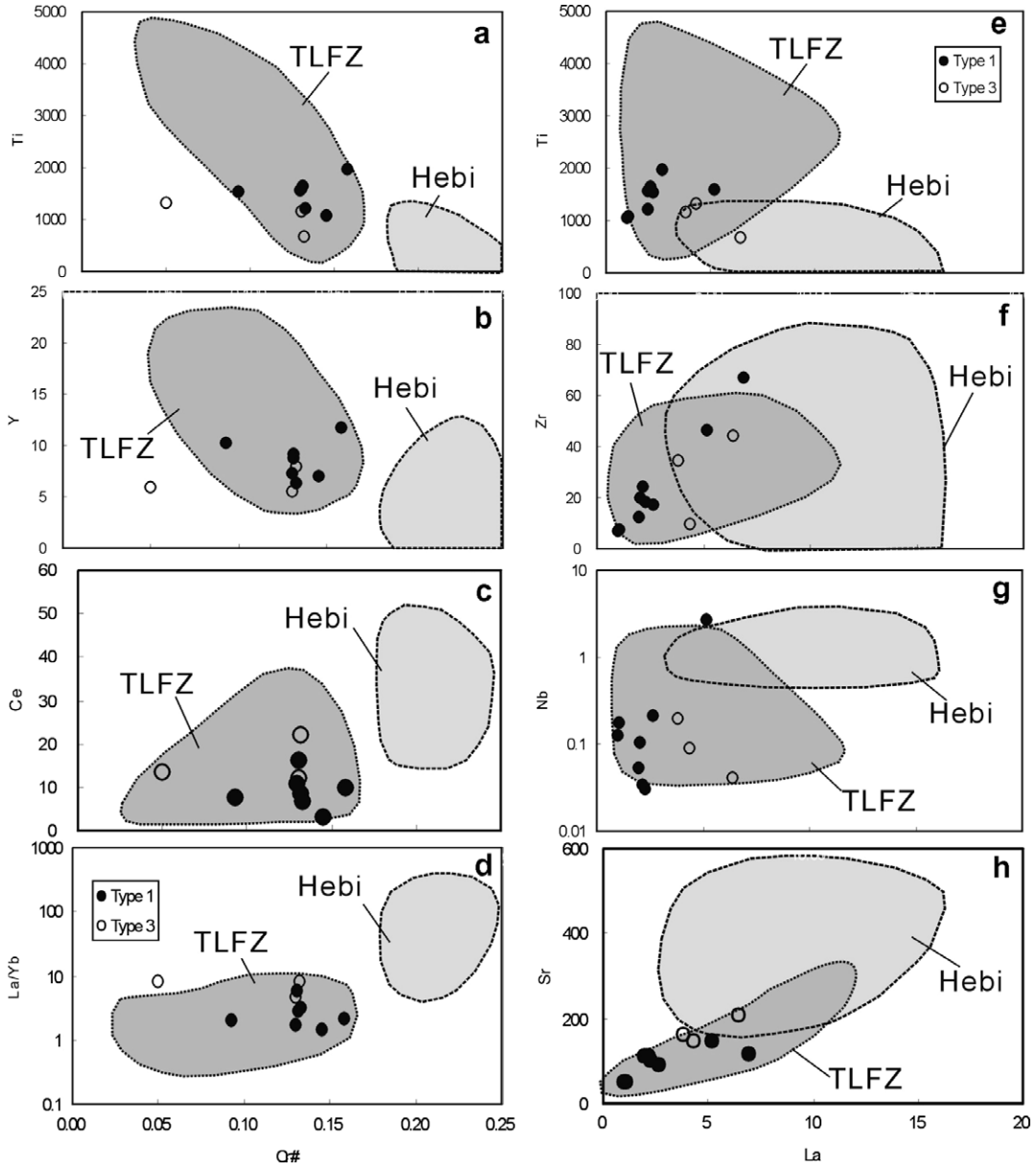

Fig. 5. Plots of $Cr^{\#}$ and La vs Ti, Y, Ce and La/Yb in clinopyroxenes from Fuxin xenoliths. Other data sources as in Fig. 3

4.4. Whole-rock composition

Compositions of the Fuxin peridotites were reconstructed using their modes (Table 1) and mineral chemistry (Table 2), because the small sample sizes did not allow bulk analysis. The reconstructed compositions show that all of the Fuxin peridotites have Al_2O_3 and CaO contents lower than the commonly accepted primitive upper mantle (PUM) compositions (McDonough and Sun, 1995). The Type 2 peridotites are highly refractory, similar to the Hebi high-Mg group peridotites. The Type 1 samples are moderately refractory to fertile, and overlap the range defined by mantle xenoliths in the TLFZ area. Type 3 peridotites have high CaO relative to Al_2O_3, plotting above the Oceanic Trend (Fig. 6a), and have markedly lower $Mg^{\#}$ values than the primitive mantle (Fig. 6b).

5. DISCUSSION

5.1. Extraction of basaltic melts in the Fuxin SCLM

Most of the clinopyroxene and spinel in the Fuxin Type 1 peridotites have $Cr^{\#}$ (e.g. 40.1 and 34.5 in JG17, respectively) in the high end of the ranges defined by these phases in xenoliths from the TLFZ. All spinels in the Type 2 and Type 3 peridotites also have high $Cr^{\#}$ values (39–59, Table 1). These data indicate that a relatively large volume of the upper SCLM has been subjected to melt extraction. Broad negative correlations between $Cr^{\#}$ and moderately incompatible elements (e.g. Y, Ti) (Fig. 5) suggest that these elements behaved similarly in the lithospheric mantle during partial melting and, therefore, can be used to model the degree of partial melting of the xenoliths (Norman, 1998).

Table 7
Temperature estimation for the Fuxin peridotite from the North China Craton (°C)

Type	Sample $P = 1.5$ GPa	T (BK) Ca in Opx	T (Wells) Opx–Cpx	T (SS, a) Opx–Cpx	T (SS, b) Sp–Opx	T (SS, c) Sp–Opx	T (WEK, a) Sp–Opx	T (WEK, b) Cr–Al–Opx
Type 1	JG6	923	931	1004	1038	975	1022	1045
	JG17	1138	1118	964	976	861	980	950
	JG18	949	948	1023	1002	902	1052	927
	JG19 (core)	888	925	906	997	889	988	995
	JG19 (rim)	1010	985	966	981	878	955	995
	JG20	956	951	872	921	841	850	986
	JG26	919	929	965	1007	907	981	1021
	JG27	993	981	974	992	828	991	973
	JG28 (core)	863	917	976	1007	866	993	1002
	JG28 (rim)	1027	1002					
	JG29	945	944	979	956	843	948	954
	JG15							
Type 2	JG23			967	900	787	867	902
	JG32			977	921	772	882	902
Type 3	JG10	964	963	1018	1008	862	1043	912
	JG12	919	941					
	JG13-1	939	935	1052	1039	796	1091	917
	JG13-2	977	970					

Notes: T (BK), Ca-in-Opx thermometer, Brey and Köhler (1990).
T (Wells), two-pryoxene thermometer, Wells (1977).
T (SS, a), T (SS, b) and T (SS, c): two-pyroxene thermometer, Sp–Opx thermometer (Fe as Fe_{Total}) and Sp–Opx thermometer (Fe as Fe^{3+}), respectively, Sachtleben and Seck (1981).
T (WEK, a) and T (WEK, b): Sp–Opx thermometer and Cr–Al–Opx thermometer, Witt-Eickschen and Seck (1991).

Modeling using Y and Yb contents in the clinopyroxene and assuming $K_d^Y = 0.42$ and $K_d^{Yb} = 0.40$ (Norman, 1998) and the primitive mantle composition (McDonough and Sun, 1995) indicates that the Type 1 samples are residues of 5–12% fractional partial melting (Fig. 7a), consistent with estimates (4.8–13.4%, Table 1) based on the spinel-$Cr^{\#}$ values using the method of Hellebrand et al. (2001). The Type 2 harzburgites are the most refractory among the Fuxin peridotites (17.0–18.7%, Table 1). The Type 3 peridotites with Low $Mg^{\#}$-olivine are intermediate between the Type 1 and 2 xenoliths, i.e. 9.5–12.5% (Cpx Y–Yb) to ~14.5% (spinel-$Cr^{\#}$ estimates). On the other hand, modeling using Ti contents and assuming $K_d^{Ti} = 0.35$ (Norman, 1998) requires even lower degrees of fractional melting (<10%; Fig. 7b). The discrepancy may reflect a later introduction of Ti during metasomatism (Norman, 1998). The modeling shows that the Fuxin Type 1 and 3 peridotites are transitional between the highly refractory relict cratonic mantle in Hebi and the fertile lithosphere in the TLFZ (Fig. 7), and that the Type 2 harzburgites are highly refractory, similar to the Hebi refractory peridotites (Zheng et al., 2001). We interpret the Type 3 xenoliths as mainly derived from the interaction of refractory mantle with the host melt.

5.2. Mantle metasomatism beneath the NCC

A range of different REE patterns is observed in mantle clinopyroxenes at many xenolith localities in the eastern NCC. The oldest samples, xenoliths and diamond inclusions from Mengyin (Zheng et al., 2006a) and Fuxian (Wang and Gasparik, 2001) and the Donghai peridotites of the Sulu orogen (Zheng et al., 2005b, 2006a), are uniformly enriched in LREE and Large Ion Lithophile Elements (LILE), even though most of these rocks have refractory major-element compositions (Fig. 8).

Xenoliths from younger localities show more variability. Flat or LREE-depleted patterns, which may record a primary depletion event, can be found in Junan (Ying et al., 2006), Hannuoba (Chen et al., 2001; Yu et al., 2006), Shanwang and Qixia (Zheng et al., 1998), Huinan and Kuandian (Xu et al., 2003; Zhang and Zheng, 2006) and Nushan (Xu et al., 1998), and occur in both fertile and transitional peridotites. The distinction between these relatively undisturbed, primitive patterns and the ubiquitous metasomatic enrichment of the SCLM seen in the older localities is further evidence that the fertile peridotites and some transitional ones represent young additions to the SCLM. However, LREE- and MREE-enriched REE patterns, coupled with high abundances of LILE, also are ubiquitous. These patterns suggest widespread secondary enrichment in the SCLM beneath the eastern North China Craton.

Enrichment in LILE and LREE has been attributed to metasomatism by carbonatitic melts (Yaxley et al., 1998), volatile-rich silicate melts (Zangana et al., 1999) or H_2O–CO_2 liquids (Stalder et al., 1998). Experimental studies of trace-element partitioning between clinopyroxene and melt in carbonate and silicate systems shows that in the carbonate system clinopyroxene-melt partition coefficients for Si, Al, heavy REE, Ti and Zr are higher by factors of 5–200 than those of the silicate system. Conversely, partition coefficients for Nb, LREE, alkali metals and alkaline earths show much less fractionation (<3; Blundy and Dalton, 2000). On the other hand, relative to silicate melt or

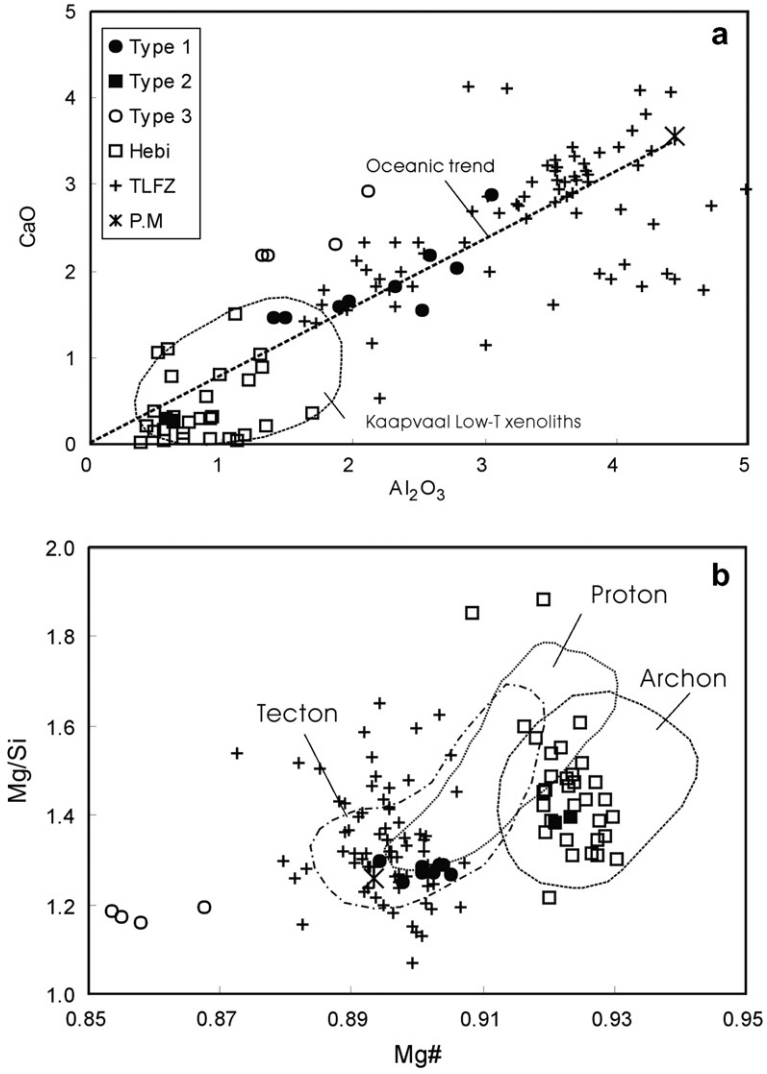

Fig. 6. Plots of CaO vs Al_2O_3 (a) and $Mg^{\#}$ vs Mg/Si in representative peridotites from eastern North China. Primitive mantle (P.M), McDonough and Sun (1995); Oceanic trend from Boyd (1996); Kaapvaal Low-T xenoliths, Boyd et al. (1993); Archean (>2.5 Ga), Proton (2.5–1.0 Ga) and Tecton (<1.0 Ga) areas, Griffin et al. (1999b); other data sources as Fig. 3.

CO_2-rich fluid, carbonatite melts can fractionate REE and HFSE more effectively and have high contents of LILE (Blusztajn and Shimizu, 1994), whereas Nb cannot be transported by H_2O-rich fluids (Eggler, 1987). Therefore, the metasomatic agent that affected the Fuxin xenoliths (except samples JG17 and JG26 with high Nb contents) is unlikely to be an H_2O-rich fluid. Ca-enrichment in spinel peridotites may reflect their equilibration with SiO_2-undersaturated melts, either carbonatite or silicate melts (Zinngrebe and Foley, 1995). This makes it difficult to constrain the nature of metasomatic agents.

However, high Ca/Al and La/Yb ratios, HFSE depletion and low Ti/Eu ratios in mantle clinopyroxenes have been widely interpreted as the key signatures of carbonatite-related metasomatism (Klemme et al., 1995; Coltorti et al., 1999). All Fuxin peridotites of Types 1 and 3, except JG13-1 (a Type 3 lherzolite), have high Ti/Eu (1700-4800) and low $(La/Yb)_n$ (<7), suggesting silicate-melt metasomatism. JG13-1 has transitional Ti/Eu and $(La/Yb)_n$, which may imply a transitional agent between carbonatitic and silicate metasomatism, or overprinting by multiple episodes of metasomatism. In fact, the majority of the Type 3 peridotites plot above the oceanic trend (Boyd, 1996) on the Al_2O_3 vs CaO diagram (Fig. 6a), also suggesting a secondary enrichment in Ca consistent with the carbonatitic metasomatism recorded by the trace-element patterns of the xenoliths.

Carbonatitic metasomatism is recorded in mantle clinopyroxenes (Fig. 9) from: (1) diamond inclusions and garnet–facies xenoliths in the Paleozoic Mengyin and Fuxian kimberlites, (2) the early Mesozoic (~220 Ma) Donghai UHP terrane peridotite and (3) the spinel–facies xenoliths in the early Mesozoic (~178 Ma) Xinyang volcanoclastic diatremes. All of the high-$Mg^{\#}$ group and part of the low-$Mg^{\#}$ group of peridotites from the Hebi basalts also record metasomatism by carbonate melts. Worldwide, this

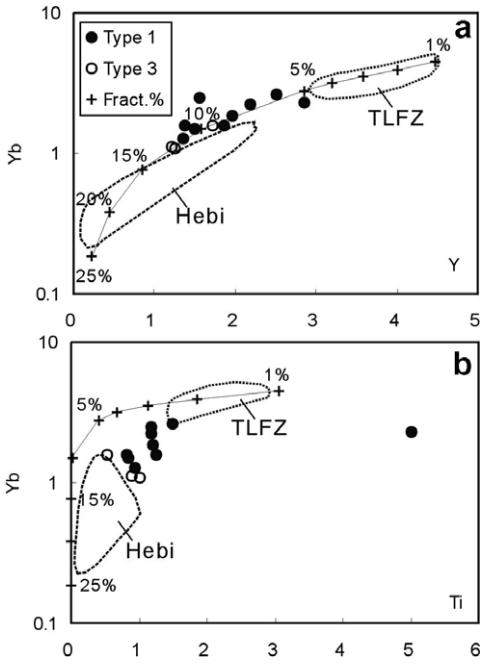

Fig. 7. Fractional melting modeling of Fuxin clinopyroxene compositions using primitive mantle-normalized abundances. Other data sources as Fig. 3.

type of metasomatism is typical of the stable cratons (Menzies, 1990). In contrast, most peridotite xenoliths from the Late Mesozoic (67 Ma) Junan basalts and the Cenozoic basalts of Hannuoba, Qixia, Nushan, Shanwang (both garnet– and spinel–facies), Huinan and Kuandian, have been affected by silicate-melt metasomatism. In several localities, such as Hannuoba and Nushan, some of the more refractory peridotites show signatures of carbonatitic metasomatism. In summary, the distribution of carbonatitic metasomatism recorded in peridotitic diopsides correlates with the regional distribution of the more refractory peridotites, and silicate metasomatism is characteristic of the more fertile lithospheric mantle. We interpret these correlations as further evidence that the refractory peridotites, and at least some of the transitional types, represent relics of the ancient SCLM.

5.3. Coexistence of refractory and fertile lithosphere

Lithospheric peridotites are represented by: (1) "cratonic" xenoliths carried in magmas (kimberlites, lamproites) that erupt through Archean lithosphere; (2) "off-craton" xenoliths carried in alkali basalts that erupted in Proterozoic and younger continental regions and (3) "massif peridotites", which are tectonic fragments of upper mantle interleaved with crustal rocks in Phanerozoic fold belts. The composition of the SCLM is broadly correlated with crustal age and/or tectonic setting (Griffin et al., 1999b), although strong reworking during the Phanerozoic assembly of an orogenic belt may make older components difficult to recognize (Griffin et al., 2000). The ranges of variation of these different mantle types can be illustrated on plots of modal olivine content vs $Mg^{\#}$ (Fig. 10). The harzburgites of the Fuxin suite (e.g. Type 2) and the Hebi high-Mg peridotites have compositions similar to refractory cratonic mantle, and this is consistent with the Archean sulfide ages of the Hebi xenoliths. In contrast, most of the Type 1 xenoliths plot within the fields of the Proterozoic and Phanerozoic lherzolites (Fig. 6b). The coexistence of refractory and fertile peridotites reflects the multi-stage evolution of the lithospheric mantle beneath the North China Craton.

A survey of published data shows that these same components can be recognized in many localities scattered in space and time across North China (Fig. 8). Mantle xenoliths from the early Paleozoic (457–500 Ma; Lu et al., 1998) Mengyin and Fuxian kimberlites in the cratonic interior are refractory garnet–facies peridotite (>92 olivine-$Mg^{\#}$) with a few transitional samples (90–92 olivine-$Mg^{\#}$). The garnet peridotites of the Donghai terrane within the Sulu orogenic belt along the southern North China Craton (e.g. CCSD-pp1) represent a moderately refractory mantle protolith (mean 91.5 olivine-$Mg^{\#}$), which experienced complex metasomatism in Mesoproterozoic time and subsolidus re-equilibration during ultrahigh-pressure (UHP) metamorphism in early Mesozoic time. These peridotites appear to represent the emplacement of solid fragments of the lithospheric mantle of the North China Craton into the top of the subducting crustal slab (Zheng et al., 2006a,c).

Mantle xenoliths from the early Mesozoic Xinyang volcanoclastic diatremes (178 Ma), in the southwestern corner of the Eastern Block of the craton, are mainly transitional but include some highly refractory peridotites. The zircon U–Pb ages of these peridotites are mainly early Mesozoic (~220 Ma), with growth and/or recrystallisation at ca. 3.2, 2.4–2.3, 1.4 and 0.7 Ga (Zheng et al., 2006b). The Early Mesozoic zircons record a metasomatic/metamorphic event, probably reflecting the release of fluids as the Yangtze crust was subducted beneath the North China Craton along the Qinling–Dabie Orogen (Zheng et al., 2005a).

All of the peridotite xenoliths in the late Mesozoic Jiaozhou (74 Ma; Yan et al., 2003) and Junan basalts (67 Ma; Ying et al., 2006) are fertile (<90 olivine-$Mg^{\#}$) except for minor transitional and refractory varieties in Junan. Peridotites in the Cenozoic Hannuoba basalts are transitional (92–90 olivine-$Mg^{\#}$) with minor proportions of refractory and fertile types (86.4–92.8, Chen et al., 2001; Yu et al., 2006). The Qixia xenoliths from the eastern part of the Tan-Lu fault zone, captured at 12 Ma, are dominantly moderately refractory with minor fertile lherzolites (Zheng et al., 1998) and give Phanerozoic whole-rock Re–Os ages (Gao et al., 2002). The peridotitic xenoliths from Hebi (4 Ma) in the interior of the craton, distant from the fault zone, are highly refractory harzburgite and Cpx-poor lherzoilte (high-Mg group) with minor transitional and fertile samples (low-Mg group). The high-Mg group represents shallow relics of the Archean cratonic mantle (Table 6), while the low-Mg group has been interpreted as newly accreted lithosphere (Zheng et al., 2001).

The Cenozoic Shanwang (16 Ma) and Nushan basalts (2 Ma) within the translithospheric Tan-Lu fault zone

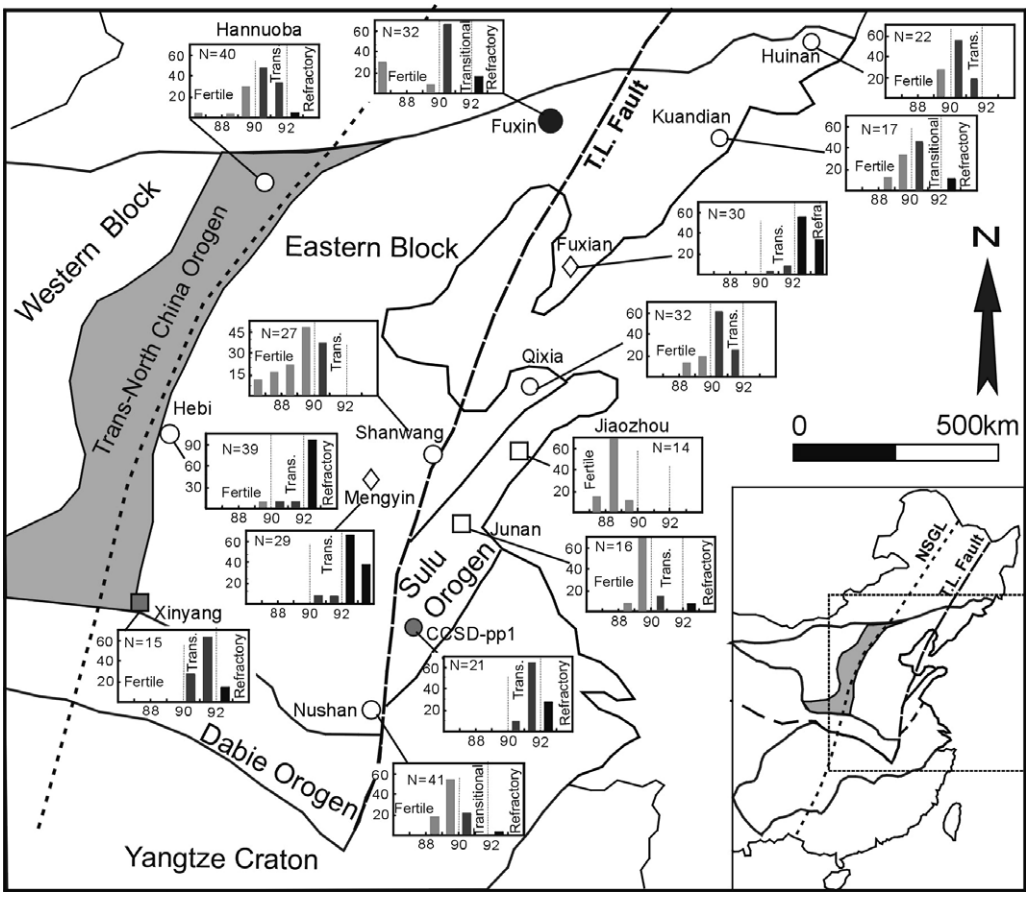

Fig. 8. Distribution of olivine-Mg# in peridotites from eastern North China. Refractory (Refra.), olivine-Mg# >92; Fertile, olivine-Mg# <90; Transitional (Trans.), olivine-Mg# 90–92. Data sources: Fuxian (Zheng, 1999); Xinyang, estimated olivine Mg# from the reflict clinopyroxene (Zheng et al., 2005a); Fusin, this paper (Table 2) and Wang et al. (2002); Jiaozhou, Yan et al. (2003); Junan, Ying et al. (2006); Hannuoba, Chen et al. (2001), Rudnick et al. (2004) and Yu et al. (2006); Shanwang, Zheng et al. (1998, 2005a, 2006a); Qixia, Zheng et al. (1998) and Rudnick et al. (2004); Hebi, Zheng et al. (2001, 2005a); Nushan, Xu et al. (1998); Huinan, Xu et al. (1996, 2003), Wu et al. (2006); Kuandian, Zhang and Zheng (2006); CCSD-pp1, Zheng et al. (2005b, 2006a,c).

(TLFZ) sampled mainly fertile xenoliths including spinel– and garnet–facies peridotites (Zheng et al., 2006a; Xu et al., 1998); minor relics of refractory mantle are found in Nushan (Fig. 1). Similarly, xenoliths from the Huinan and Kuandian basalts, erupted at 1–3 Ma in the northeastern parts of the craton, captured mainly transitional (moderately refractory) lherzolites with minor amounts of fertile and/or refractory types; these peridotites give Paleoproterozoic to Phanerozoic whole-rock Re–Os ages (Wu et al., 2003, 2006).

The distribution of fertile versus transitional and refractory peridotites within the lithospheric mantle at each locality may be examined using histograms of their equilibration temperatures (Fig. 11). At most localities the three types overlap to a significant extent. This survey indicates that refractory, transitional and fertile peridotites coexisted in the SCLM beneath many localities during Mesozoic to Quaternary time. Available whole-rock and sulfide Re–Os T_{RD} model ages (Table 6; Xu et al., 2007) suggest that the most refractory components are relics of an Archean SCLM. This is also consistent with the preservation of Archean U–Pb ages in zircons in peridotite xenoliths from Xinyang. However, the transitional peridotites analysed so far show no sign of Archean ages; they retain Proterozoic ages, overprinted by younger generations of sulfides. They may reflect Proterozoic modification of ancient SCLM, or generation of new, less depleted SCLM during Proterozoic consolidation of the craton (Gao et al., 2002). In contrast, most fertile peridotites yield either Phanerozoic T_{RD}, or "future" ages that may reflect a higher mean Re/Os in the SCLM since Neoproterozoic time (Xu et al., 2007).

Fertile peridotites are rare in the xenolith suites from the Paleozoic Mengyin and Fuxian kimberlites. In the xenolith suites from Mesozoic–Tertiary basalts, the proportion of fertile peridotites is clearly highest in some localities near the translithospheric Tan-Lu fault zone, while more refractory components are more commonly preserved in more distant localities such as Hebi, Fuxin and Kuandian (Fig. 8). This distribution, and the pattern of Re–Os ages, suggests that the fertile lherzolites represent material generated in post-Paleozoic time, and that major translithospheric structures such as the Tan-Lu fault zone have played a role in the replacement of the ancient SCLM with more fertile material. This apparently gradual modification of the

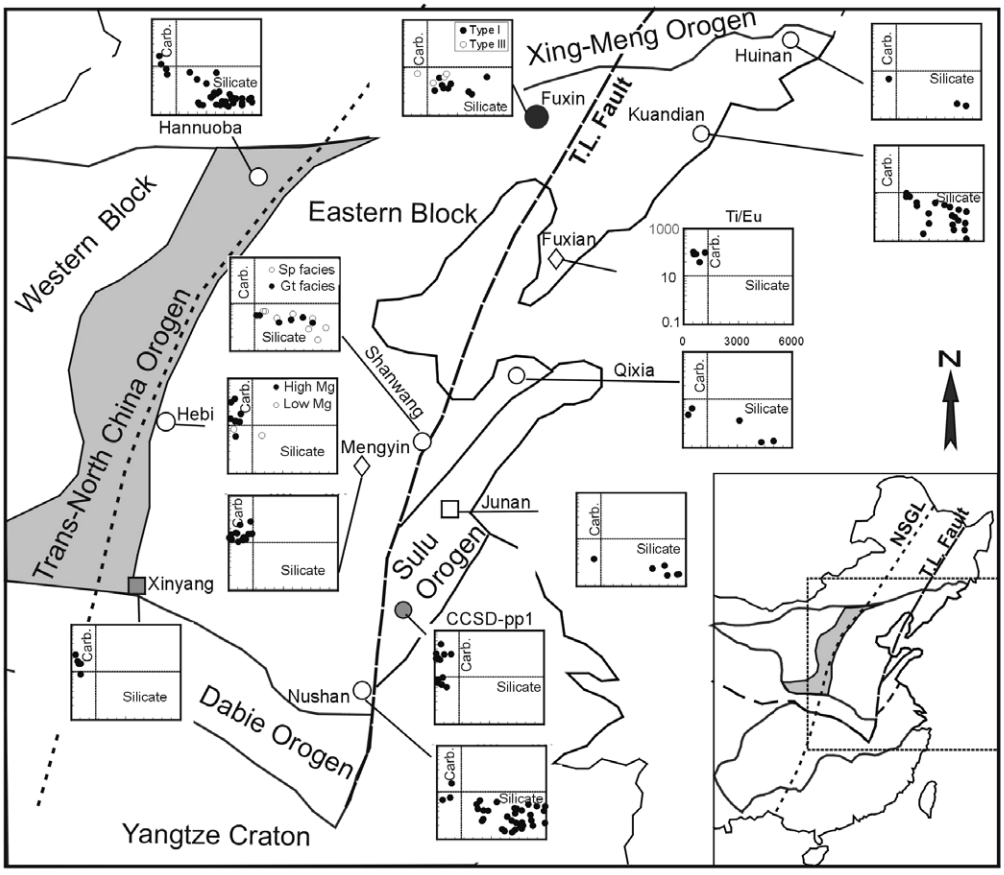

Fig. 9. Distribution of mantle metasomatism signatures (Ti/Eu vs La/Yb) in Cpx of peridotites from eastern North China. Signatures of silicate and carbonatitic metasomatism modified after Coltorti et al. (1999). Other data sources: Diamond inclusions, Zheng (1999); Mengyin, Zheng et al. (2006a); Donghai, Zheng et al. (2005b, 2006a); Xinyang, Zheng et al. (2005a); Junan, Ying et al. (2006); Hannuoba, Chen et al. (2001) and Yu et al. (2006); Shanwang sp–facies, Zheng et al. (1998); Shanwang grt–facies, Zheng et al. (2006a); Qixia, Zheng et al. (1998); Hebi (high- and low-Mg groups), Zheng et al. (2001); Nushan, Xu et al. (1998); Huinan and Kuandian, Zhang and Zheng (2006).

lithospheric mantle cannot be well explained by a sudden lithospheric delamination (Deng et al., 2004; Gao et al., 2004; Wu et al., 2006), thus a more continuous chemical process is more likely.

5.4. Lithospheric thinning and mantle replacement

Archean Re–Os depletion ages for the highly refractory peridotites in the diamondiferous Fuxian and Mengyin kimberlites (Gao et al., 2002; Zhang et al., 2007b) and the barren Tieling kimberlites (Wu et al., 2006) show that a thick cratonic SCLM (garnet–facies) formed in Archean time, and persisted beneath parts of the North China Craton at least until Early Paleozoic time (Zheng and Lu, 1999). Similar ages (Table 6) for peridotitic sulfides in the Hebi basalts indicate that shallow relics of this highly refractory mantle have survived until Neogene time (4 Ma) at least locally within the interior of the North China Craton. In contrast, abundant Proterozoic ages in the marginal parts of the craton, such as Hannuoba on the northern edge (Table 6; also see Gao et al., 2002; Xu et al., 2007) and Xinyang on the southern edge (Zheng et al., 2005a) suggest that the lithospheric mantle in these areas was generated, or strongly modified, in Paleoproterozoic time. The Hf model ages of zircons from the Donghai CCSD-pp1 peridotite within the Sulu UHP Orogen (Zheng et al., 2006c) are also Proterozoic. These peridotite massifs are interpreted as fragments of the lithospheric mantle from beneath the North China Craton. We therefore suggest that the subcontinental lithospheric mantle, at least around the marginal parts of the craton, were refertilized or modified through the interaction of peridotite with melts and fluids derived from asthenospheric mantle in Proterozoic times. On the other hand, the widespread distribution of Phanerozoic fertile SCLM, either unmetasomatised or affected by silicate-melt metasomatism, in the eastern part of the craton and especially along the translithospheric Tan-Lu fault zone, seems to require another mechanism.

The North China Craton may have been more easily affected by subduction and collision with surrounding blocks, due to its small size compared to many other cratons worldwide. In Early Mesozoic time, the subduction of the Yangtze Craton beneath the southern margin of the North China Craton may have resulted not only in a lateral spreading of the lithosphere beneath the North China Craton (Zheng et al., 2006a,c), but also in mantle-wedge

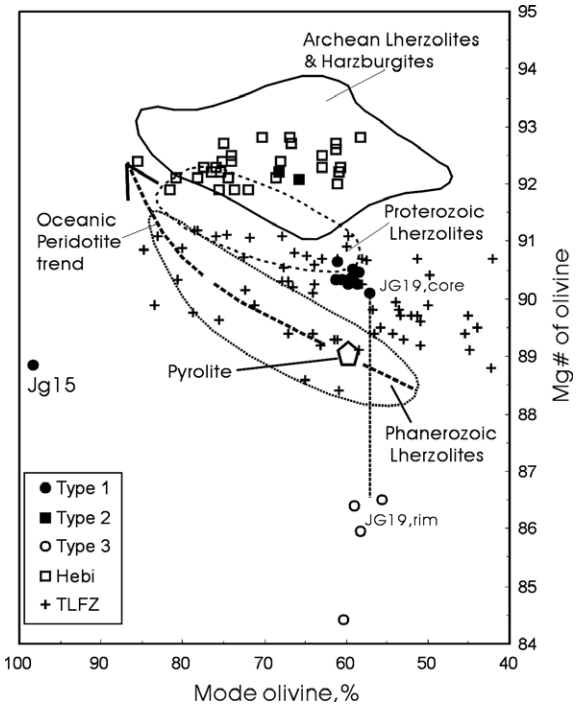

Fig. 10. Plots of modal olivine (%) vs $Mg^{\#}$ of representative mantle peridotites from eastern North China. Archean, Proterozoic and Phanerozoic areas are from Griffin et al. (1999b). Other data sources as Fig. 5.

metasomatism by fluids and/or melts derived from the subducted continental crust (Zheng et al., 2005a). Zhang et al. (2003) and Zhang (2005) suggested that melt–peridotite interaction was the primary mechanism for transformation of the lithosphere from a cratonic refractory mantle to more fertile compositions. However, it is difficult to imagine that the cratonic mantle, with its complex history, could be converted to 'oceanic'-type lithosphere with an apparently simpler history through a melt–peridotite reaction. Although melt-related metasomatism could produce a general refertilization of the depleted SCLM in elements such as Ca, Fe and Al (Beyer et al., 2006), it is difficult to imagine a melt or fluid that can transform refractory mantle clinopyroxenes with enrichment in LREE but low HREE contents (high La/Yb) to fertile ones with depletion in LREE but high HREE contents (low La/Yb). These considerations led Zheng et al. (2005a) to argue that the lithospheric thinning beneath the eastern North China Craton in Late Mesozoic–Cenozoic included the upwelling and the cooling of asthenospheric mantle to form a new, fertile lithosphere (Fan and Menzies, 1992; Xu et al., 1995b; Zheng et al., 1998).

Based on detailed seismic tomography, Zheng and Lu (1996) and Yuan (1996) presented a "mushroom cloud" model to explain the dramatic change in the nature of the SCLM in the eastern part of the North China Craton during late Mesozoic–Cenozoic times (Zheng, 1999; Lu et al., 2000). In this model, old cold lithospheric mantle has been pulled apart during extension, and hot new material derived from the upwelling asthenosphere has risen along the major faults, spreading laterally in the upper part of the subcontinental lithospheric mantle. This model is consistent with the tendency for refractory peridotites to occur at greater depths (higher T) in many localities. The model implies that the mantle beneath the translithospheric Tan-Lu fault is dominantly Phanerozoic in character and represents the newly accreted material that replaced the older lithosphere through extension, thermal erosion and metasomatism. The translithospheric Tan-Lu fault (and other subparallel fault zones) thus has played an important part in the Mesozoic–Cenozoic replacement of the pre-existing Archean/Proterozoic lithospheric mantle (Zheng et al., 1998, 2001; Gao et al., 2002; Zhang et al., 2004). The upwelling of asthenospheric material resulted in the irregular emplacement of hot fertile mantle material, accompanied by the infiltration of asthenosphere-derived melts, along the weak zones in the old lithospheric mantle (Fig. 12). However, this replacement was not necessarily synchronous everywhere but heterogeneously distributed in space and time, and might have occurred over a long time.

Yan et al. (2003) constrained the minimum age of the mantle replacement by the occurrence of fertile peridotite xenoliths in the Late Mesozoic (74 Ma) Jiaozhou basalts. Peridotites from this study indicate that such replacement had occurred before 100 Ma beneath Fuxin (Fig. 12). A still older minimum age (~125 Ma; also see Xu et al., 2004) for the replacement is suggested by the eruption of the earliest tholeiitic basalts e.g. the Yixian Formation in the Yanshan intracontinental orogen within the craton (Lu et al., 2006) and the Fangcheng basalts within a small Mesozoic sedimentary basin in Feixian County of western Shandong Province (Zhang et al., 2002, 2007a). The cooling of the upwelling asthenosphere since 100 Ma ago would lower the boundary between lithosphere and asthenosphere and achieve the partial replacement of the old refractory lithospheric mantle by newly accreted fertile material. Once this replacement had occurred, and upwelling had subsided, the elevated advective geotherms associated with the asthenospheric upwelling would begin to relax toward more typical conductive conditions. Under these conditions, the subcontinental lithospheric mantle column would be denser than before, and would start to sink to form basins. Kaminski and Jaupart (2000) have proposed a similar mechanism for the formation of the Phanerozoic intracratonic basins in North America, although they invoked interaction between plumes and the SCLM to change the density of the SCLM column.

The sedimentary basins of eastern North China have formed in two episodes, one in the Jurassic–Cretaceous and the second in the Eocene (Ren et al., 2002). These periods coincide with two peaks of heat flow calculated from coal reflectivity (R_o) measurements in the Songliao and North China Basins: 99 mW/m^2 at 115 Ma and 87 mW/m^2 at 57 Ma (Li, 1995). These thermal episodes may have accompanied asthenospheric upwelling, and may be related to subduction of the Kula Plate in Jurassic–Cretaceous time and the Pacific Plate in the Tertiary (Menzies et al., 1993; Griffin et al., 1998b; Zheng et al., 2006a). Thus, the Jurassic–Cretaceous and Eocene could be the most important

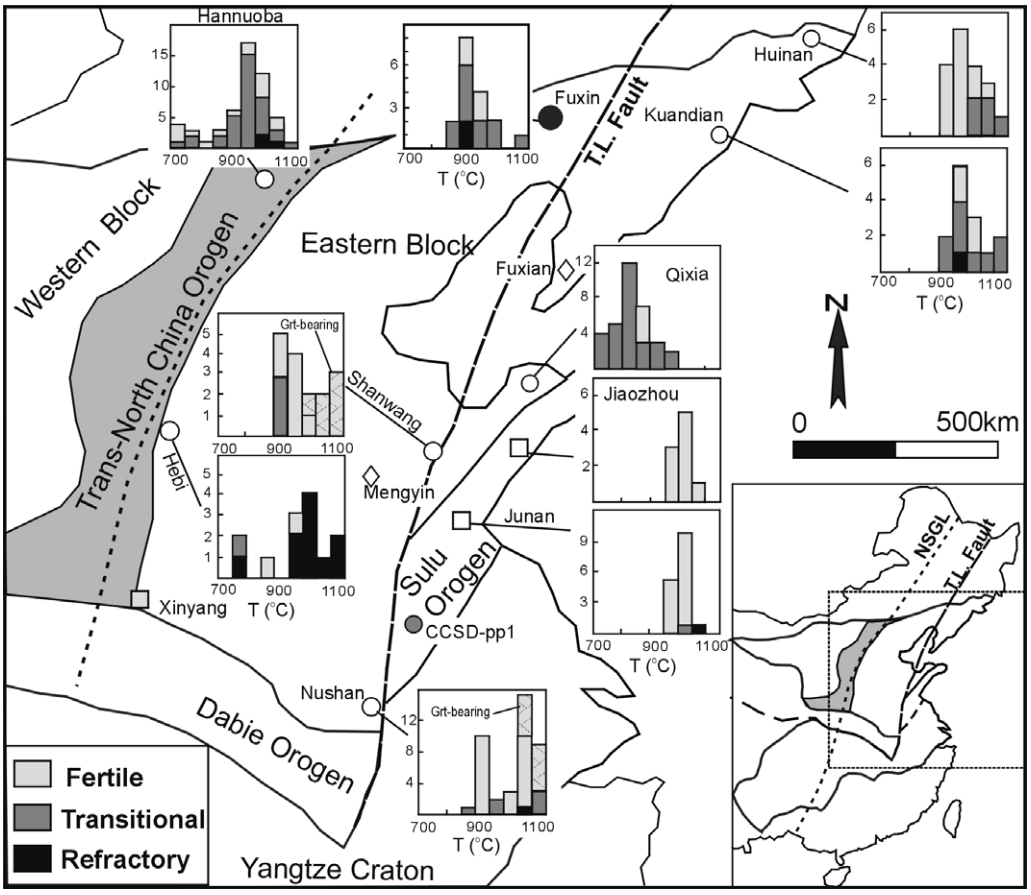

Fig. 11. Two-pyroxene equilibration temperatures of peridotites in eastern North China. Temperatures calculated using the Brey and Köhler (1990) calibration at 1.5 GPa for the sp–facies peridotites except for two Fuxin harzburgites (Type 2) using the Witt-Eickschen and Seck (1991). Other data sources: Jiaozhou—Yan et al. (2003); Junan—Ying et al. (2006); Hannuoba—Song and Frey (1989), Fan and Hooper (1989), Chen et al. (2001), Rudnick et al. (2004) and Yu et al. (2006); Shanwang—Zheng et al. (1998, 2006a); Qixia—Zheng et al. (1998) and Rudnick et al. (2004); Hebi—Zheng et al. (2001); Huinan and Kuandian—Wu et al. (2006), Zhang and Zheng (2006); Nushan—Xu et al. (1998).

periods in the modification and replacement of the lithospheric mantle.

6. CONCLUSIONS

1. Late Mesozoic (~100 Ma) lithospheric mantle beneath the eastern North China Craton (e.g. Fuxin) is composed of major lherzolites with ~90 olivine $Mg^{\#}$ and minor magnesian (>92 $Mg^{\#}$ olivine) harzburgite and ferrous (~86 $Mg^{\#}$ olivine) lherzolites. The dominant fertile lherzolites ($F\% = 5$–12% are similar to the fertile mantle sampled by many are widespread beneath Late Mesozoic–Cenozoic (<74 Ma) basalts, and record silicate-melt metasomatism. The harzburgites represents relics of the ancient cratonic mantle; similar rocks are found in several localities across the craton. The ferrous lherzolites are interpreted as the products derived from interaction of the lithosphere with magmas similar to the host basalts.
2. In-situ Re–Os data on sulfides in Cenozoic xenoliths from Hebi (4 Ma) and Hannuoba (22 Ma) within the North China Craton have T_{RD} populations at 3.1–3.0, 2.5, 2.2–2.1, 1.4 and 0.8 Ga, corresponding to the U–Pb ages of zircons from early Mesozoic (178 Ma) peridotitic xenoliths at the southern margin of the craton. These ages record events during which the Archean lithospheric mantle was modified, reflecting a long and complex evolution of the cratonic root.
3. Lithosphere thinning and the partial replacement of the refractory lithospheric mantle by more fertile material was heterogeneously distributed in space and time. Lateral spreading of the lithosphere, accompanied by asthenospheric upwelling and melt-peridotite interaction, is the most probable mechanism for the modification of the Archean lithospheric root beneath the eastern part of the North China Craton.
4. Subsequent cooling of the upwelled asthenosphere resulted in an overall more fertile and hence denser lithosphere, resulting in widespread basin formation as the lithosphere cooled. The dominance of fertile peridotite xenoliths in the 100 Ma Fuxin basalts indicates that the mantle replacement beneath the eastern North China Craton began before that time, while basin analysis suggests that it has continued into Tertiary time.

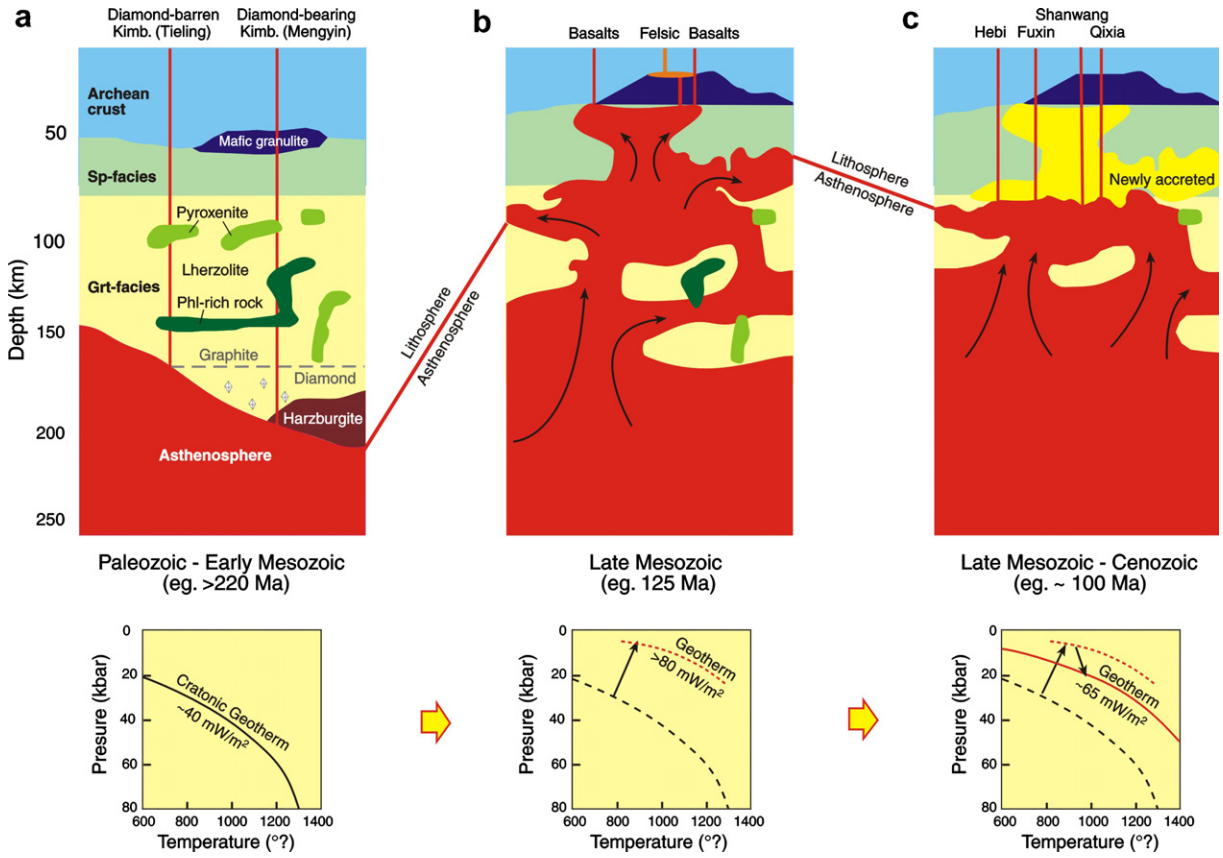

Fig. 12. Cartoon illustrating a model for Late Mesozoic–Cenozoic lithospheric thinning and mantle replacement beneath the eastern North China Craton. (a) Paleozoic–Early Mesozoic (e.g. $\geqslant$220 Ma): Mengyin kimberlites are generated ($\sim$500 Ma) from the base of a thick cratonic lithosphere with a low geotherm ($\sim$40 mW/m^2). This mantle was partly disrupted during the Yangtze collision and subsequent exhumation (e.g. 220–178 Ma), with possible lithospheric spreading in early Mesozoic (Zheng et al., 2006a); (b) $\sim$125 Ma: asthenospheric upwelling, probably related to subduction of the Kula Plate in Late Jurassic–Cretaceous time, erodes the remaining lithospheric mantle with Archean and Proterozoic ages; (c) Late Mesozoic–Cenozoic (e.g. $\sim$100 Ma): asthenospheric cooling lowers the boundary between the lithosphere and the asthenosphere and creates new lithospheric mantle, derived from the upwelling asthenosphere; eruption of Cenozoic alkali basalts. Asthenospheric upwelling, related to subduction of the Pacific Plate in the Tertiary, erodes the lithospheric mantle including newly accreted lithosphere (e.g. Type 1) and the relict cratonic mantle (e.g. Type 2). Subsequent cooling leads to widespread basin formation.

ACKNOWLEDGMENTS

The authors thank the journal editor Frank A Podosek, associate editor Martin Menzies and three reviewers (Yigang Xu, Anton Ie Roex and an anonymous reviewer) for their constructive comments and suggestions. We are grateful for Ms. Suzy Elhou for assistance with the analytical work. This study was supported by the Chinese Nature Science Funding (40425002, 90714002, 40521001 and 40673002), ARC Discovery and Linkage grants and the ACILP AusAID Program (S.Y.O'R. and W.L.G.). The analytical work used instrumentation funded by ARC LIEF and DEST Systemic Infrastructure Grants, Macquarie University and Industry. This is Contribution No. 493 from the ARC National Key Centre for the Geochemical Evolution and Metallogeny of Continents (www.els.mq.edu.au/GEMOC/).

REFERENCES

Beyer E., Griffin W. L. and O'Reilly S. Y. (2006) Transformation of Archean lithospheric mantle by refertilisation: evidence from exposed peridotite in the Western Gneiss Region, Norway. *J. Petrol.* **47**, 1611–1634.

Blundy J. and Dalton J. (2000) Experimental comparison of trace element partitioning between clinopyroxene and melt in carbonate and silicate systems, and implications for mantle metasomatism. *Contrib. Mineral. Petrol.* **139**, 356–371.

Blusztajn J. and Shimizu N. (1994) The trace-element variations in clinopyroxenes from spinel peridotite xenoliths from southwest Poland. *Chem. Geol.* **111**, 227–243.

Boyd F. R. (1996) Origin of peridotite xenoliths: major element consideration. In *High Pressure and High Temperature Research on Lithosphere and Mantle materials* (eds. G. Ranalli, F. Ricci Lucchi, C. A. Ricci and T. Trommosdorff). University of Siena, Siena, pp. 89–106.

Boyd F. R., Pearson D. G., Nixon P. H. and Mertzman S. A. (1993) Low-calcium garnet harzburgites from southern Africa: their relations to craton structure and diamond crystallization. *Contrib. Mineral. Petrol.* **113**, 352–366.

Brey G. and KÖhler T. (1990) Geothermobarometry in four-phase lherzolites. II: New thermobarometers and practical assessment of existing thermobarometers. *J. Petrol.* **31**, 1352–1378.

Chen S. H., O'Reilly S. Y., Zhou X. H., Griffin W. L., Zhang G. H., Sun M., Feng J. L. and Zhang M. (2001) Thermal and

petrological structure of the lithosphere beneath Hannuoba, Sino-Korean craton, China: evidence from xenoliths. *Lithos* **56**, 267–301.

Coltorti M., Bonadiman C., Hinton R. W., Siena F. and Upton B. G. (1999) Carbonatite metasomatism of the oceanic upper mantle: evidence from clinopyroxenes and glasses in ultramafic xenoliths of Grande Comore, Indian Ocean. *J. Petrol.* **40**, 133–165.

Deng J. F., Mo X. X., Zhao H. L. and Luo Z. H. (2004) A new model for the dynamic evolution of Chinese lithosphere: continental roots-plume tectonics. *Earth Sci. Rev.* **65**, 223–275.

Eggler D. H. (1987) Solubility of major and trace elements in mantle metasomatic fluids: experimental constraints. In *Mantle Metasomatism* (eds. M. A. Menzies and C. J. Hawkesworth). Academic Press Geology Series, London, pp. 21–41.

Fan Q. C. and Hooper P. R. (1989) The mineral chemistry of ultramafic xenoliths of Eastern China: implications for upper mantle composition and the paleogeotherms. *J. Petrol.* **30**, 1117–1158.

Fan W. M. and Menzies M. A. (1992) Destruction of aged lower lithosphere and accretion of asthenosphere mantle beneath eastern china. *Geotect. Metallogen.* **16**, 171–179.

Fan W. M., Zhang H. F., Baker J., Jarvis K. E., Mason P. R. D. and Menzies M. A. (2001) On and off the North China craton: where is the Archean keel? *J. Petrol.* **41**, 933–950.

Gao S., Rudnick R. L., Carlson R. W., McDonough W. F. and Liu Y. S. (2002) Re–Os evidence for replacement of ancient mantle lithosphere beneath the North China craton. *Earth Planet. Sci. Lett.* **198**, 307–322.

Gao S., Rudnick R. L., Yuan H. L., Liu X. M., Liu Y. S., Xu W. L., Ling W. L., Ayers J., Wang X. C. and Wang Q. H. (2004) Recycling lower continental crust in the North China craton. *Nature* **432**, 892–897.

Griffin W. L., O'Reilly S. Y. and Ryan C. G. (1992) Composition and thermal structure of the lithosphere beneath South Africa, Siberia and China: Proton microprobe studies. *International Symposium on Cenozoic Volcanic Rocks and Deep-seated Xenoliths of China and its Environs*, Beijing, p. 20.

Griffin W. L., Zhang A. D., O'Reilly S. Y. and Ryan C. G. (1998b) Phanerozoic evolution of the lithosphere beneath the Sino-Korean craton. In *Mantle Dynamics and Plate interactions in east Asia. Amer. Geodynamics*, Vol. 27 (eds. M. Flower, S. L. Chung, C. H. Lo and Y. Y. Lee). American Geophysical Union, Washington, DC, pp. 107–126.

Griffin W. L., O'Reilly S. Y. and Ryan C. G. (1999b) The composition and origin of sub-continental lithospheric mantle. In *Mantle Petrology: Field Observations and High-pressure Experimentation: A tribute to Francis R. (Joe) Boyd* (eds. Y. Fei, C. M. Berka and B. O. Mysen). The Geochemical Society, Special Publication 6, pp. 13–45.

Griffin W. L., Pearson N. J., Belousova E., Jackson S. E., O'Reilly S. Y., van Achterberg E. and Shee S. R. (2000) The Hf isotope composition of cratonic mantle: LAM-MC-ICPMS analysis of zircon megacrysts in kimberlites. *Geochim. Cosmochim. Acta* **64**, 133–147.

Harte B. (1977) Chemical variations in upper mantle nodules from southern African kimberlites. *J. Petrol.* **85**, 279–288.

Hellebrand E., Snow J. E., Dick H. J. B. and Hofmann A. W. (2001) Coupled major and trace elements as indicators of the extent of melting in mid-ocean-ridge peridotites. *Nature* **410**, 677–681.

Kaminski E. and Jaupart C. (2000) Lithosphere structure beneath the Phanerozoic intracratonic basins of North America. *Earth Planet. Sci. Lett.* **178**, 139–149.

Klemme S., van der Laan S. R., Foley S. F. and Gunther D. (1995) Experimentally determined trace and minor element partitioning between clinopyroxene and carbonatite melt under upper mantle conditions. *Earth Planet. Sci. Lett.* **133**, 439–448.

Le Maitre R. W. (1982) *A classification of igneous rocks and glossary of terms*. Blackwell Scientific Publications, London.

Li Z. A. (1995) The evolution characters of mantle heat flow beneath Songliao basin. *Geotect. Metallogen.* **19**, 108–112, in Chinese.

Liu D. Y., Nutman A. P., Compston W., Wu J. S. and Shen Q. H. (1992) Remnants of 3800 Ma crust in Chinese part of the Sino-Korean craton. *Geology* **20**, 339–342.

Lu F. X., Wang Y., Chen M. H. and Zheng J. P. (1998) Geochemical characteristics and emplacement ages of the Mengyin kimberlites, Shandong Province, China. *Int. Geol. Rev.* **40**, 998–1006.

Lu F. X., Zheng J. P., Li W. P., Chen M. H. and Chen Z. M. (2000) The mantle evolution pattern of Phanerozoic mantle in the eastern China: the "mushroom cloud" model. *Earth Science Frontiers* **7**, 97–107, in Chinese.

Lu F. X., Zheng J. P., Shao J. A., Zhang R. S., Chen M. H. and Yu C. M. (2006) Asthenospheric upwelling and lithospheric thinning in late Cretaceous–Cenozoic in eastern North China. *Geosci. Front.* **13**, 86–92, in Chinese.

McDonough W. F. and Sun S. S. (1995) The composition of the Earth. *Chem. Geol.* **120**, 223–253.

Menzies M. A. (1990) *Continental mantle*. Clarendon Press, Oxford, p. 184.

Menzies M. A., Fan W. M. and Zhang M. (1993) Paleozoic and Cenozoic lithoprobes and loss of >120 km of Archean lithosphere, Sino-Korean craton, China: magmatic processes and plate tectonics. *Geol. Soc. Spec. Publ.* **76**, 71–81.

Menzies M. A. and Xu Y. G. (1998) Geodynamics of the North China Craton. In *Mantle Dynamics and Plate Internationals in East Asia* (eds. M. Flower, S. L. Chung and C. H. Lo). Am. Geophys. Union Geodyn. Ser., 27, pp. 155–165.

Menzies M., Xu Y. G., Zhang H. F. and Fan W. M. (2007) Integration of geology, geophysics and geochemistry: a key to understanding the North China Craton. *Lithos* **96**, 1–21.

Norman M. D., Pearson N. J., Sharma A. and Griffin W. L. (1996) Quantitative analysis of trace elements in geological materials by laser ablation ICPMS: instrumental operating conditions and calibration values of NIST glasses. *Geostand. Newslett.* **20**, 247–261.

Norman M. D. (1998) Melting and metasomatism in the continental lithosphere: Laser ablation ICPMS analysis of minerals in spinel lherzolites from eastern Australia. *Contrib. Mineral. Petrol.* **130**, 240–255.

O'Reilly S. Y., Griffin W. L., Poudjom Y. H. and Morgan P. (2001) Are lithosphere forever? Tracking changes in subcontinental lithospheric mantle through time. *GSA Today* **11**, 4–10.

O'Reilly S. Y., Chen D., Griffin W. L. and Ryan C. G. (1996) Minor element in olivine from spinel lherzolite xenoliths: implications for thermobarometry. *Mineral. Mag.* **61**, 257–269.

Pearson N. J., Alard O., Griffin W. L., Jackson S. E. and O'Reilly S. Y. (2002) In situ measurement of Re–Os isotopes in mantle sulfides by laser ablation multicollector-inductively coupled plasma mass spectrometry: analytical methods and preliminary results. *Geochim. Cosmochim. Acta* **66**, 1037–1050.

Pearson D. G. (1999) The age of continental roots. *Lithos* **48**, 171–194.

Pouchou J. L. and Pichoir F. (1984) A new model for quantitative X-ray microanalysis. Part 1: Application to the analysis of homogeneous samples. *Recherche Aerospat.* **5**, 13–38.

Ren J. Y., Tamaki K., Li S. T. and Zhang J. X. (2002) Late Mesozoic and Cenozoic rifting and its dynamic setting in Eastern China and adjacent areas. *Tectonophysics* **344**, 175–205.

Rudnick R. L., Gao S., Ling W. L., Liu Y. S. and McDonough W. F. (2004) Petrology and geochemistry of spinel peridotite xenoliths from Hannuoba and Qixia, North China craton. *Lithos* **77**, 609–637.

Sachtleben T. and Seck H. A. (1981) Chemical control of Al-solubility in orthopyroxene and its implications on pyroxene geothermometry. *Contrib. Mineral. Petrol.* **78**, 157–165.

Shirey S. B. and Walker R. J. (1998) The Re–Os isotope system in cosmochemistry and high temperature geochemistry. *Annu. Rev. Earth Planet. Sci.* **26**, 423–500.

Song Y. and Frey F. A. (1989) Geochemistry of peridotite xenoliths in basalt from Hannuoba, Eastern China: implications for subcontinental mantle heterogeneity. *Geochim. Cosmochim. Acta* **53**, 97–113.

Stalder R., Foley S. F., Brey G. P. and Horn I. (1998) Mineral-aqueous fluid partitioning of trace elements at 900-1200 °C and 3.0–5.7 GPa: new experimental data for garnet, clinopyroxene, and rutile, and implications for mantle metasomatism. *Geochim. Cosmochim. Acta* **62**, 1781–1801.

van Achterbergh E., Ryan C., Jackson S. and Griffin. W. (2001) Appendix 3 Data reduction software for LA-ICP-MS. In *Laser-Ablation-ICPMS in the Earth Sciences* (ed. P. Sylvester), vol. 29. Mineralogical Association of Canada Short Course, pp. 239–243.

Wang W. Y. and Gasparik T. (2001) Metasomatic clinopyroxene inclusions in diamonds from the Liaoning province, China. *Geochim. Cosmochim. Acta* **65**, 611–620.

Wang D. Y., Xu W. L. and Feng H. (2002) Nature of late Mesozoic lithospheric mantle in western Liaoning province: Evidences from basalt and the mantle-derived xenoliths. *J. Jilin Univ.* **32**, 319–324, in Chinese.

Wells P. R. A. (1977) Pyroxene thermometry in simple and complex systems. *Contrib. Mineral. Petrol.* **62**, 129–139.

Witt-Eickschen G. and Seck H. A. (1991) Solubility of Ca and Al in orthopyroxene from spinel peridotite: an improved version of an empirical geothermometer. *Contrib. Mineral. Petrol.* **106**, 431–439.

Wu F. Y., Walker R. J., Ren X. W., Sun D. Y. and Zhou X. H. (2003) Osmium isotopic constraints on the age of lithospheric mantle beneath northeastern China. *Chem. Geol.* **196**, 107–129.

Wu F. Y., Walker R. J. and Yang Y. H. (2006) The chemical-temporal evolution of lithospheric mantle underlying the North China Craton. *Geochim. Cosmochim. Acta* **70**, 5013–5034.

Xu J. W., Zhu G., Tong W. X., Cui K. R. and Liu Q. (1987) Formation and evolution of the Tancheng–Lujiang wrench fault system: A major shear system to the northwest of the Pacific Ocean. *Tectonophysics* **134**, 273–310.

Xu W. L., Zheng C. Q. and Wang D. Y. (1999) Discovery of mantle- and lower crust-derived xenoliths in Mesozoic trachybasalts from Western Liaoning, and their geological implications. *Geol. Rev.* **45**, 444–449.

Xu X. S., O'Reilly S. Y., Griffin W. L. and Zhou X. (1998) The nature of the Cenozoic lithosphere at Nushan, eastern China. In *Mantle Dynamics and Plate Internationals in East Asia* (M. Flower, S. L. Chung and C. H. Lo), vol. 27. Am. Geophys. Union Geodyn. Ser., pp.167–196.

Xu X. S., Griffin W. L., O'Reilly S. Y., Pearson N. J., Cheng, H.and Zheng J. P. (2007) Re–Os isotopes in mantle xenoliths from eastern China: Age constraints and evolution of the lithospheric mantle. *Lithos* (in press).

Xu Y. G., Lin C. Y., Shi L. B., Mercier J.-C. C. and Ross J. V. (1995a) Upper mantle geotherm for eastern China and its geological implications. *Sci. China B* **38**, 1482–1492.

Xu Y. G., Fan W. M. and Lin G. (1995b) Lithosphere-asthenosphere interaction: a comparative study on Cenozoic and Mesozoic basalts around Bohai area. *Geotect. Metallogen.* **19**(4), 1–13.

Xu Y. G., Lin C. Y. and Menzies M. A. (1996) Mineral chemistry of minerals in spinel peridotite xenoliths from Wangqing of Jilin Province: thermal history and metasomatism of upper mantle. *J. Geochem.* **25**, 481–493, in Chinese.

Xu Y. G., Huang X. L. and Thirlwall M. F. (2003) 'Reactive' harzburgite xenoliths from Huinan, Jilin Province and their implication for deep dynamic processes. *Acta Petrol. Sin.* **19**, 19–26, in Chinese.

Xu Y. G., Huang X. L., Ma J. L., Wang Y. B., Xu J. F., Wang Q. and Wu X. Y. (2004) Crustal–mantle interaction during the thermotectonic reactivation of the North China Craton: SHRIMP zircon U–Pb age, petrology and geochemistry of Mesozoic plutons in western Shandong. *Contrib. Mineral. Petrol.* **147**, 750–767.

Xu Y. G. (2001) Thermo-tectonic destruction of the Archean lithospheric keel beneath the Sino-Korean craton in China: evidence, timing and mechanism. *Phys. Chem. Earth A* **26**, 747–757.

Xu Y. G. (2007a) Diachronous lithospheric thinning of the North China Craton and formation of the Daxinánling–Taihangshan gravity lineament. *Lithos* **69**, 281–298.

Yan J., Chen J. F. and Xie Z. (2003) Mantle xenoliths from Late Cretaceous basalt in eastern Shandong Province: New constraint on the timing of lithospheric thinning in eastern China. *Chin. Sci. Bull.* **48**, 2139–2144.

Yaxley G. M., Green D. H. and Kamenetsky V. (1998) Carbonatite metasomatism in the southeastern Australia lithosphere. *J. Petrol.* **39**, 1917–1930.

Ying J. F., Zhang H. F., Kita N., Morishita Y. and Shimoda G. (2006) Nature and evolution of Late Cretaceous lithospheric mantle beneath the eastern North China Craton: constraints from petrology and geochemistry of peridotitic xenoliths from Junan, Shandong Province, China. *Earth Planet. Sci. Lett.* **244**, 622–638.

Yu C. M., Zheng J. P. and Griffin W. L. (2006) LAM-ICPMS analysis on clinopyroxene of peridotite xenoliths from Hannuoba and its significance on lithospheric mantle evolution. *Earth Sci.* **31**, 93–100, in Chinese.

Yuan X. C. (1996) *Atlas of geophysical in China*. Geological Publishing House, Beijing, p. 217.

Zangana N. A., Downes H., Thirlwall M. F., Marriner G. F. and Bea F. (1999) Geochemical variation in peridotite xenoliths and their constituent clinopyroxenes from Ray Pic (French Massif Central): implications for the composition of the shallow lithospheric mantle. *Chem. Geol.* **153**, 11–35.

Zhang H. F., Sun M., Zhou X. H. and Lu F. X. (2002) Mesozoic lithosphere destruction beneath the North China Craton: Evidence from major-, trace-element and Sr–Nd–Pb isotope studies of Fangcheng basalts. *Contrib. Mineral. Petrol.* **144**, 241–253.

Zhang H. F., Sun M., Zhou X. H., Zhou M. F., Fan W. M. and Zheng J. P. (2003) Secular evolution of the lithosphere beneath the eastern North China Craton: Evidence from Mesozoic basalts and high-Mg andesites. *Geochim. Cosmochim. Acta* **67**(22), 4373–4387.

Zhang H. F. and Zheng J. P. (2003) Geochemical characteristics and petrogenesis of Mesozoic basalts from the North China Craton: a case study in Fuxin, Liaoning Province. *Chin. Sci. Bull.* **48**, 924–930.

Zhang H. F., Ying J. F., Xu P. and Ma Y. G. (2004) Mantle olivine xenocrysts entrained in Mesozoic basalts from the North China craton: implication for replacement process of lithospheric mantle. *Chin. Sci. Bull.* **49**, 961–966.

Zhang H. F. (2005) Transformation of lithospheric mantle through peridotite-melt reaction: a case of Sino-Korean craton. *Earth Planet. Sci. Lett.* **237**, 768–780.

Zhang H. F., Ying J. F., Shimoda G., Kita N. T., Morishita Y., Shao J. A. and Tang Y. J. (2007a) Importance of melt circulation and crust-mantle interaction in the lithospheric evolution beneath the North China Craton: evidence from Mesozoic basalt-borne clinopyroxene xenocrysts and pyroxenite xenoliths. *Lithos* **96**, 67–89.

Zhang H.F., Goldstein S.L., Zhou X.H., Sun M., Zheng J.P. and Cai Y. (2007b) Evolution of subcontinental lithospheric mantle beneath eastern China: Re-Os isotopic evidence from mantle xenoliths in Paleozoic kimberlites and Mesozoic basalts. *Contrib. Mineral. Petrol.* (in press).

Zhang Z. H. and Zheng J. P. (2006) Cenozoic lithospheric mantle in Huinan and Kuandian areas. *Geol. Sci. Technol. Inform.* **25**, 9–16, in Chinese.

Zhao G. C., Wilde S. A., Cawood P. A. and Lu L. Z. (1999) Thermal evolution of two textural types of mafic granulites in the North China craton: evidence for both mantle plume and collisional tectonics. *Geol. Mag.* **136**, 223–240.

Zheng J. P. and Lu F. X. (1996) Paleo-mantle fluid and its significance in cratonic evolution: Taking the North China platform as an example. *Earth Science Frontiers* **3**, 187–194, in Chinese.

Zheng J. P., O'Reilly S. Y., Griffin W. L., Lu F. X. and Zhang M. (1998) Nature and evolution of Cenozoic lithospheric mantle beneath Shandong Peninsula, Sino-Korean craton. *Int. Geol. Rev.* **40**, 471–499.

Zheng J. P. (1999) *Mesozoic–Cenozoic mantle replacement and lithospheric thinning*. China University of Geosciences Press, Wuhan, East China, in Chinese, p. 126.

Zheng J. P. and Lu F. X. (1999) Mantle xenoliths from kimberlites, Shandong and Liaoning: Paleozoic lithospheric mantle character and its heterogeneity. *Acta Petrol. Sin.* **15**, 65–74, in Chinese.

Zheng J. P., O'Reilly S. Y., Griffin W. L., Lu F. X., Zhang M. and Pearson N. J. (2001) Relics of refractory mantle beneath the eastern North China block: significance for lithosphere evolution. *Lithos* **57**, 43–66.

Zheng J. P., Griffin W. L., O'Reilly S. Y., Lu F. X., Wang C. Y., Zhang M., Wang F. Z. and Li H. M. (2004a) 3.6 Ga lower crust in central China: new evidence on the assembly of the North China Craton. *Geology* **32**, 229–232.

Zheng J. P., Griffin W. L., O'Reilly S. Y., Lu F. X. and Yu C. M. (2004b) U–Pb and Hf-isotope analysis of zircons in mafic xenoliths from Fuxian kimberlites: evolution of the lower crust beneath the North China Craton. *Contrib. Mineral. Petrol.* **148**, 79–103.

Zheng J. P., Sun M., Zhou M. F. and Robinson P. (2005a) Trace elemental and PGE geochemical constraints of Mesozoic and Cenozoic peridotitic xenoliths on lithospheric evolution of the North China Craton. *Geochim. Cosmochim. Acta* **69**, 3401–3418.

Zheng J. P., Zhang R. Y., Griffin W. L., Liou J. G. and O'Reilly S. Y. (2005b) Heterogeneous and metasomatised mantle recorded by trace elements in minerals of the Donghai garnet peridotites, Sulu UHP terrane, China. *Chem. Geol.* **221**, 243–259.

Zheng J. P., Griffin G. L., O'Reilly S. Y., Yang J. S., Li T. F., Zhang M., Zhang R. Y. and Liou J. G. (2006a) Mineral chemistry of peridotites from Paleozoic, Mesozoic and Cenozoic lithosphere: Constraints on mantle evolution beneath Eastern China. *J. Petrol.* **47**, 2233–2256.

Zheng J. P., Griffin W. L., O'Reilly S. Y., Zhang M. and Pearson N. (2006b) Zircons in mantle xenoliths record the Triassic Yangtze—North China continental collision. *Earth Planet. Sci. Lett.* **247**, 130–142.

Zheng J. P., Griffin W. L., O'Reilly S. Y., Yang J. S. and Zhang R. Y. (2006c) A refractory mantle protolith in younger continental crust, east-central China: Age and composition of zircon in the Sulu UHP peridotite. *Geology* **34**, 705–708.

Zinngrebe E. and Foley S. F. (1995) Metasomatism in mantle xenoliths from Gees, west Eifel, Germany: evidence for the genesis of calc-alkaline glasses and metasomatic Ca-enrichment. *Contrib. Mineral. Petrol.* **122**, 79–96.

Associate editor: Martin A. Menzies